Genome Biology

RESEARCH

Open Access

Trans-regulation of heterochromatin underlies genetic variation in 3D genome contacts in mouse embryonic stem cells

Haley J. Fortin[1,2], Anna Z. Struba[1], Arad Bustan[1,3] and Christopher L. Baker[1,2,3*]

*Correspondence:
christopher.baker@jax.org

[1] The Jackson Laboratory, Bar Harbor, ME 04609, USA
[2] Graduate School of Biomedical Sciences, Tufts University, Boston, MA 02111, USA
[3] Graduate School of Biomedical Science and Engineering, University of Maine, Orono, ME 04469, USA

Abstract

Background: Genetic variation drives phenotypic diversity and disease susceptibility. *Trans*-acting genetic variation coordinates genome-wide chromatin changes, yet the molecular mechanisms underlying this distal regulation remain unclear. Here, we use the power of mouse genetics to investigate how genetic variation at *trans*-acting loci regulates three-dimensional (3D) chromatin interactions.

Results: Using HiChIP to map chromatin contacts among regulatory elements in C57BL/6J and DBA/2J embryonic stem cells (ESCs), we identify 4,962 strain-differential interactions. Of these, 71% overlap chromatin accessibility quantitative trait loci (QTL), establishing that interaction variation is predominantly heritable. These differential interactions show coordinated changes in chromatin state and gene expression, with stronger interactions associated with increased accessibility and transcription. Notably, loci regulated in *trans* exhibit a unique chromatin signature where weaker interactions are enriched for H3K9me3-marked heterochromatin. Analysis of F1 hybrids reveal dominant repressive effects, consistent with heterochromatin-mediated *trans*-regulation. To causally test this mechanism, we generate reciprocal congenic mouse strains swapping a *trans*-QTL region. Integrated multiomic profiling of congenic ESC lines demonstrates that this locus coordinates H3K9me3, H3K27ac, chromatin accessibility, and 3D contacts at hundreds of regulatory elements, with 73–94% validating directional predictions from QTL mapping. The functional impact of heterochromatin deposition is confirmed by corresponding changes in *trans*-regulated gene expression.

Conclusions: This work establishes heterochromatin formation as a defining feature of *trans*-regulation in mouse embryonic stem cells, providing a framework for understanding how genetic variation in early developmental chromatin states could generate phenotypic diversity while preserving essential developmental programs.

Keywords: 3D genome organization, Embryonic stem cells, Epigenetics, Genetics, Genomics

Background

In humans, genetic variation has a profound impact on normal health and disease. The majority of loci associated with variation in complex traits are concentrated in *cis* regulatory elements (CREs), such as promoters, enhancers, and insulators, rather than coding regions [1–3]. Of interest, many of these regulatory elements are active during early development [1, 4], suggesting potential developmental origins of adult diseases. CRE activity is modulated through DNA and histone modifications, chromatin accessibility, and three-dimensional (3D) genome architecture [5–8]. Given that 99% of the human genome is non-coding, understanding how genetic variation influences CREs is critical for deciphering genome function [9, 10], normal development, and, when these processes goes awry, the etiology of developmental disorders and disease.

Sequence variation can alter gene expression locally in *cis*, i.e., on the same chromosome (Chr), or distally, on another chromosome, in *trans*. *Cis*-regulatory variants affect nearby genes through changes in local CREs, whereas *trans*-regulatory effects are mediated by diffusible factors, often thought of as transcription factors (TFs) or chromatin regulators, that can act on many CREs throughout the genome [11]. There is a growing interest in addressing how *trans*-regulation impacts complex traits and disease [12–18]. While effect sizes, tissue-specificity, and multiple testing burden similarly challenge both human and mouse mapping studies [15, 16], the reduced power to detect *trans* quantitative trait loci (QTL) in human cohorts is largely driven by allele frequency. Rare variants often exhibit larger effects but require very large sample sizes for detection, whereas common variants, that typically exhibit weaker effects, can be mapped with smaller cohorts [19–21]. In contrast, mapping populations such as the mouse Diversity Outbred (DO) and BXD recombinant inbred panel effectively make rare variants common, enabling more powerful mapping of *trans*-QTL [22–25]. Using the BXD recombinant inbred panel, whose parental strains C57BL/6J (B6) and DBA/2J (D2) differ at over 5,000,000 single nucleotide variants (SNVs) [26], we previously identified both *cis*- and *trans*-QTL regulating chromatin accessibility, histone modifications, and gene expression in mouse embryonic stem cells (mESCs) and male germ cells [27, 28]. In ESCs, we mapped several *trans*-QTL hotspots that regulate coordinated changes in both chromatin accessibility and gene expression, impacting gene networks important for pluripotency and cell fate determination [28]. Interestingly, genes associated with development and disease have also been independently mapped to closely overlapping intervals within a QTL on Chr13 [27, 29–33]. This Chr13 QTL contains a cluster of KRAB zinc-finger proteins (KZFPs), known transcriptional repressors that act in *trans* to establish heterochromatin. Despite success in identifying *trans*-QTL in both mice and humans [27, 28, 34–36], their mode of action remain poorly understood.

Chromosome conformation capture (3C) technologies [37–42] have revealed regulatory roles for 3D genome organization in gene expression [43–48], from regulatory loops connecting CREs to their target genes [49–52] to topologically associated domains [53–55]. Local genetic variation alters 3D genome structure in *cis*, helping determine how SNVs are associated with disease risk [56] and how structural variants (SVs) impact development of disorders ranging from rheumatoid arthritis and sex reversal to limb malformations [57–59]. Systems genetic approaches have also identified how genetic variation among human lymphoblastoid cell lines influences diverse features

of chromatin state and 3D contacts [60]. While these studies have established how *cis*-acting genetic variants disrupt 3D chromatin organization, the mechanisms by which *trans*-acting genetic variation alters 3D contacts remain largely unexplored. Even when *trans*-QTL are detected, the molecular mechanisms by which single genetic loci coordinate chromatin state changes at hundreds of distal genomic regions are largely unknown. Understanding these mechanisms is essential for interpreting how genetic variation influences complex traits and disease susceptibility, and the contribution of variation to early developmental regulation.

Here, we investigated molecular mechanisms underlying *trans*-regulation of 3D genome organization. Using HiChIP to map H3K27ac-associated chromatin interactions in B6 and D2 mouse embryonic stem cells (mESCs), we identified that contact anchors of differential interactions (DIs) substantially overlapped QTL targets associated with chromatin accessibility (caQTL) and gene expression (eQTL). Integrated epigenomic profiling revealed that heterochromatin formation distinguished *trans* from *cis* regulatory mechanisms. To causally test this mechanism, we generated reciprocal congenic strains, each isogenic to its respective parental background except for the Chr13 *trans*-QTL interval, enabling independent validation of predicted chromatin changes in both directions. Multiomic profiling of congenic mESCs validated that this *trans*-acting locus coordinates chromatin state at hundreds of distal regulatory loci with high concordance. Together, these findings establish *trans*-regulation through heterochromatin formation as a key mechanism that coordinates changes in the regulatory landscape.

Results

Genetic variation alters chromatin interactions and coordinates gene expression

To investigate how genetic variation impacts 3D genome architecture at CREs, we performed HiChIP [39] on mESC lines derived from B6 and D2 embryos. HiChIP was performed using the histone modification H3K27ac to enrich for 3D interactions at active enhancers. In total, this approach identified a combined set of 90,098 high-confidence interactions across both genetic backgrounds, defined as those spanning greater than 5 kb, a false discovery rate (FDR) < 0.01, and supported by at least four paired-end tag (PET) counts in at least two samples. Independently derived replicate lines from the same strain showed high concordance, while between-strain comparisons revealed reduced concordance, indicating that genetic background, rather than line-specific variation, drives chromatin organization differences (Fig. 1a and Additional file 1: Fig. S1a). These interactions predominantly connected enhancers to promoters (e-p, 84%), or enhancers to other enhancers (e-e, 14%). To understand the functional impact of 3D contacts, we integrated RNA-seq data previously collected from the same ESCs [28]. We observed that gene expression at connected promoters increases with increasing number of chromatin interactions (All pairwise comparisons Tukey $p < 2e\text{-}16$; Fig. 1b), consistent with previous findings [61, 62]. Furthermore, genes annotated for "stem cell population maintenance" (MGI GO:0019827) are enriched among the upper quartile of connected genes (Fisher's Exact Test $p < 0.032$), consistent with the observation that highly connected genes represent cell type–specific function [9, 63]. Among the 90,098 high-confidence interactions, the number of DIs between B6 and D2 ESCs varied with FDR threshold, ranging from 1.9% to 5.5% of total interactions (Additional file 4: Table S1). To

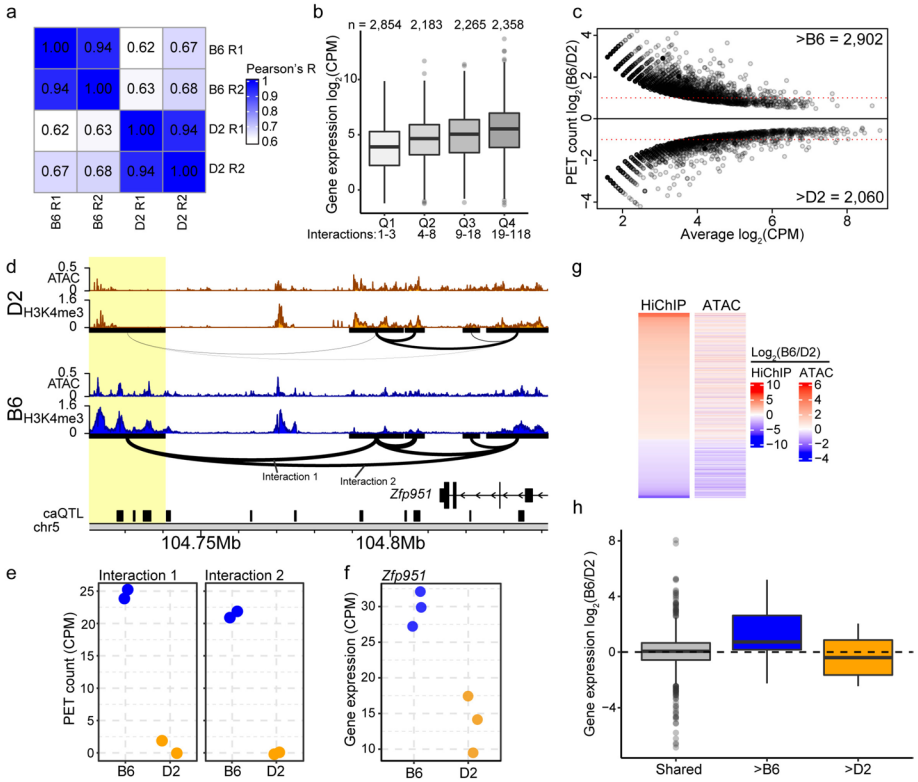

Fig. 1 Genetic variation coordinates chromatin interactions, accessibility, and gene expression. **a** Pearson correlation of H3K27ac HiChIP from biological replicates (R1 and R2) of mouse embryonic stem cells (ESCs) derived from B6 and D2 strains. **b** Box and whisker plots indicating mean gene expression values from RNA-seq for B6 and D2 mESCs (for all figure boxes: first quartile, median, and third quartile, whiskers: minimum and maximum, outliers are indicated as dots). Genes were stratified into quartiles (Q1-4) based on the number of contacts per promoter (interactions below graph, gene number above). One-way ANOVA: $F_{(3, 9656)} = 232$, $p < 2e\text{-}16$; Tukey HSD post-hoc test: all pairwise comparisons between quartiles were significant. **c** MA-plot for differential interactions B6 and D2 ESCs (FDR < 0.2). **d** Genome browser profiles of H3K4me3 ChIP-seq and ATAC-seq at the *Zfp951* locus for B6 (blue) and D2 (orange). DIs are drawn below H3K4me3 tracks. The thickness of the arc connecting two anchors represent contact frequency. Black boxes represent chromatin accessibility regions mapped as quantitative trait loci (caQTL) [28]. Yellow highlight – contact anchor overlapping multiple QTL targets. **e** HiChIP PET counts for B6 and D2 from interactions 1 ($p = 7.44e\text{-}9$) and 2 ($p = 4.48e\text{-}10$) at *Zfp951* locus. **f** Expression of *Zfp951* from B6 and D2 ESCs ($p = 2.81e\text{-}5$). **g** Heatmap indicating fold-change (B6/D2) in HiChIP PET counts for DIs (left) and corresponding fold-change for ATAC-seq signal at peaks that overlap contact anchors (right). **h** Box and whisker plots of fold-change (B6/D2) in RNA-seq signal at genes which overlap contact anchors for interactions without significant differences (shared, $n = 943$), and either greater in B6 ($n = 17$) or D2 ($n = 6$)

increase the number of DIs available for downstream overlap and comparative analyses, we used a relaxed threshold (Benjamini–Hochberg corrected $p < 0.2$, n = 4,962; Fig. 1c). We note that H3K27ac HiChIP measures contacts at regions marked by H3K27ac; differential signals may therefore reflect changes in contact frequency, H3K27ac enrichment, or both. To validate differential interactions independent of H3K27ac status we performed 3C-qPCR [64] at three loci that represent 10 DIs encompassing both B6 and D2 high interactions. This enrichment-free approach confirmed the directional trends of strain-specific interaction patterns (Additional file 1: Figs. S2-S4).

Differential chromatin interactions between B6 and D2 ESCs correspond with coordinated changes in chromatin accessibility and gene expression. The *Zfp951* locus provides

an example of coordinated regulation. Specifically, B6 shows higher PET counts at both e-e (Interaction 1) and e-p (Interaction 2) interactions compared to D2 (Fig. 1d, e). Increased 3D contacts in B6 are consistent with higher epigenetic marks associated with increased CRE activity (e.g., chromatin accessibility and H3K4me3 enrichment) in the loop anchor region (Fig. 1d yellow highlight) and higher *Zfp951* expression in B6 (Fig. 1f). This pattern suggests a shared regulatory mechanism coordinating changes in CRE activity, 3D contacts, and gene expression. Genome-wide, DIs showed coordinated strain-specific changes in both chromatin accessibility and interaction strength (Fisher's Exact Test $p < 2.2e\text{-}16$; Fig. 1g). The strain-specific bias seen for *Zfp951* expression generally holds for all DIs (Fig. 1h); chromatin interactions that are stronger in either B6 or D2 coincide with higher expression of anchor-connected genes. In contrast, genes connected to non-DIs, such as the housekeeping gene *Gapdh*, showed minimal expression bias ($\log_2$(B6/D2) = 0.05; Fig. 1h, Additional file 1: Fig. S1b, c). Together, these data demonstrate that genetic variation coordinately modulates CRE activity, 3D interaction strength, and expression of interacting genes, but leaves open the question of the mechanism of regulation.

Genetic variation regulates chromatin interactions through both cis- and trans-acting mechanisms

To test whether coordinated changes in chromatin state and gene expression reflect shared genetic control, we determined if DI anchors are enriched for genetically-regulated CREs by examining overlap with previously identified caQTL targets [28]. For instance, both gene expression of *Zfp951* and accessibility of an upstream CRE (Chr5:104,727,903 bp) were mapped to the same Chr5 locus (Fig. 2a, b, c), with B6 haplotypes conferring higher activity. In total, five interaction anchors contacting *Zfp951* overlap eight caQTL all showing higher B6 accessibility [28], demonstrating that individual anchors can harbor multiple caQTL targets. This pattern extends genome-wide; 71.7% of DI anchors are enriched for caQTL targets at one (42.6%) or both (29.1%) anchors. To test whether this overlap exceeds chance expectation, we performed permutation testing by randomizing anchor positions while preserving regional genomic structure. Observed overlap significantly exceeded permuted expectations (Z = 11.06 one and 40.34 both; $p < 0.001$; Fig. 2d; Additional file 1: Fig. S1d, e). Notably, this enrichment is robust to FDR threshold; at FDR < 0.05, enrichment for caQTL targets at both anchors increases to 40.1% (Z = 81.68, $p < 0.001$; Additional file 4: Table S2), indicating that our relaxed threshold captures additional true positives rather than introducing substantial noise. These data indicate that contact frequency at anchors for most DIs is under genetic regulation, and suggest that genetic regulation coordinates both chromatin accessibility and 3D genome structure.

Given QTL target enrichment at DI anchors, we tested whether parental interaction strength in B6 and D2 correlates with QTL effect sizes measured across the BXD panel [28]. When stratifying by QTL class, *trans*-QTL were conservatively defined as those mapping to a different chromosome than the target peak, while *cis*- mapped to the same chromosome. Interaction strength showed moderate but highly significant positive correlation with chromatin accessibility at *cis* (Pearson r = 0.41, $p = 1.4e\text{-}105$) and *trans* (r = 0.45, $p = 7.1e\text{-}100$) caQTL targets (Fig. 2e, f). We further explored the link

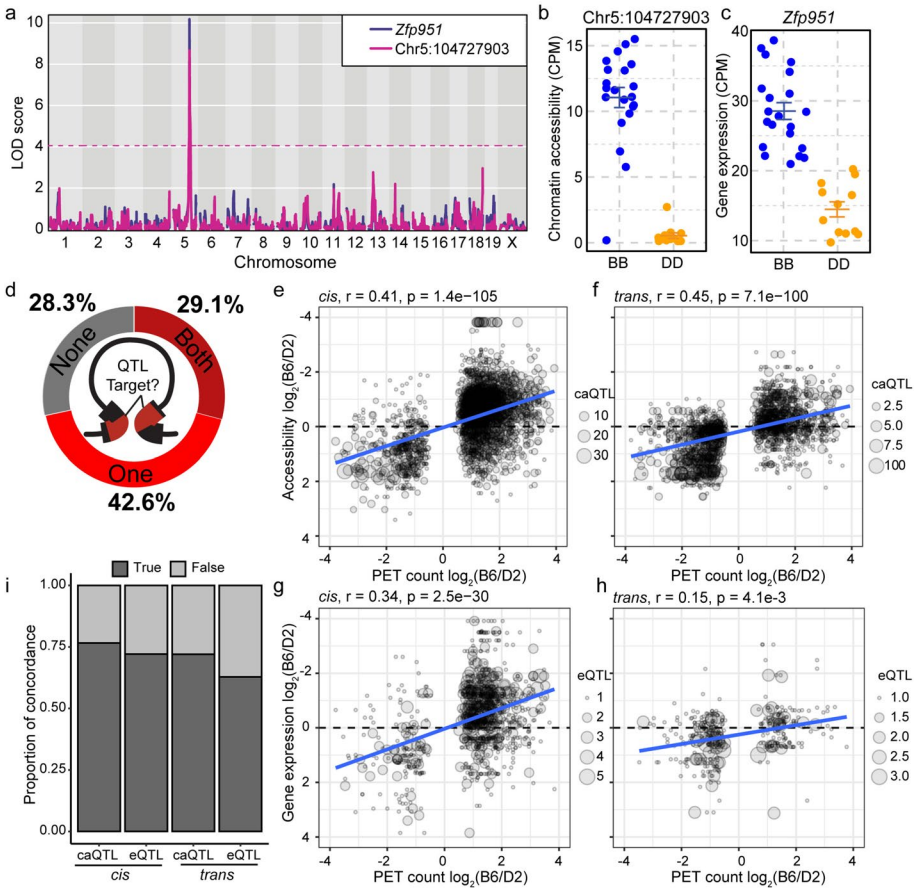

Fig. 2 Differential interactions overlap QTL targets and show allelic concordance. **a** LOD score plot for *Zfp951* and CRE (Fig. 1d, leftmost caQTL target in highlighted anchor). Both chromatin accessibility and expression of *Zfp951* are regulated locally on Chr 5. **b** Chromatin accessibility at *Zfp951* CRE (Fig. 2a pink line) in 33 BXD ESC lines based on genotype at the QTL (line represents mean ± standard error). **c** Gene expression of *Zfp951* in 33 BXD ESC lines. **d** Donut plot indicating proportions of DIs for which contact anchors overlap caQTL targets at one, both, or no anchors. Correlation between PET count and chromatin accessibility (**e**, **f**) or gene expression (**g**, **h**), separated into *cis*- (left) and *trans*-associations (right). **i** Proportion of allele concordance between interaction strength and chromatin accessibility (ca-) or gene expression (e-) QTL targets. *cis* caQTL: $\chi^2 = 529.5$, df = 2, $p < 2.2e\text{-}16$; *trans* caQTL: $\chi^2 = 440.2$, df = 2 $p < 2.2e\text{-}16$; *cis* eQTL: $\chi^2 = 148.2$, df = 1 $p < 2.2e\text{-}16$; *trans* eQTL $\chi^2 = 20.3$, df = 1 = 6.7e-6

between 3D contacts and gene regulation (Fig. 2g, h) and identified a similar correlation at *cis* (r = 0.34, p = 2.5e-30) and *trans* (r = 0.15, p = 4.1e-3) eGenes. Beyond correlation magnitude, directional concordance provides stronger evidence for coordinated regulation; loci where the B6 allele shows higher interaction strength might be expected to exhibit B6-biased molecular phenotypes. Indeed, at the categorical level, we found significant allele concordance between interaction strength and chromatin accessibility or gene expression at both *cis*- and *trans*-QTL targets (Fig. 2i, Pearson's Chi-squared test all $p < 6.7e\text{-}6$). The high allelic concordance between 3D architecture, chromatin accessibility, and gene expression at both *cis*- and *trans*-QTL targets suggests shared regulatory mechanisms coordinate these molecular layers. Moreover, the presence of *trans*-acting effects indicates that diffusible chromatin regulators mediate long-range genetic control of chromatin organization.

Heterochromatin formation regulates trans-acting chromatin interactions

While both *cis* and *trans*-QTL targets showed coordinated effects on chromatin accessibility and 3D interactions, the molecular mechanism distinguishing these regulatory modes remained unclear. We hypothesized that distinct mechanisms underlie *trans* and *cis* regulation. To test this, we examined enrichment of DNA-binding factors at interaction anchors that overlap *trans*-regulated loci (i.e., *trans*-QTL targets). Supporting our previous observations [28], we identified TRIM28 (KAP1) as the most highly enriched factor at *trans*-QTL targets (Fig. 3a). Given TRIM28's role in establishing heterochromatin through H3K9me3 deposition [65, 66], we hypothesized that *trans*-targets would show enrichment for repressive chromatin marks. Specifically, at *trans*-QTL targets

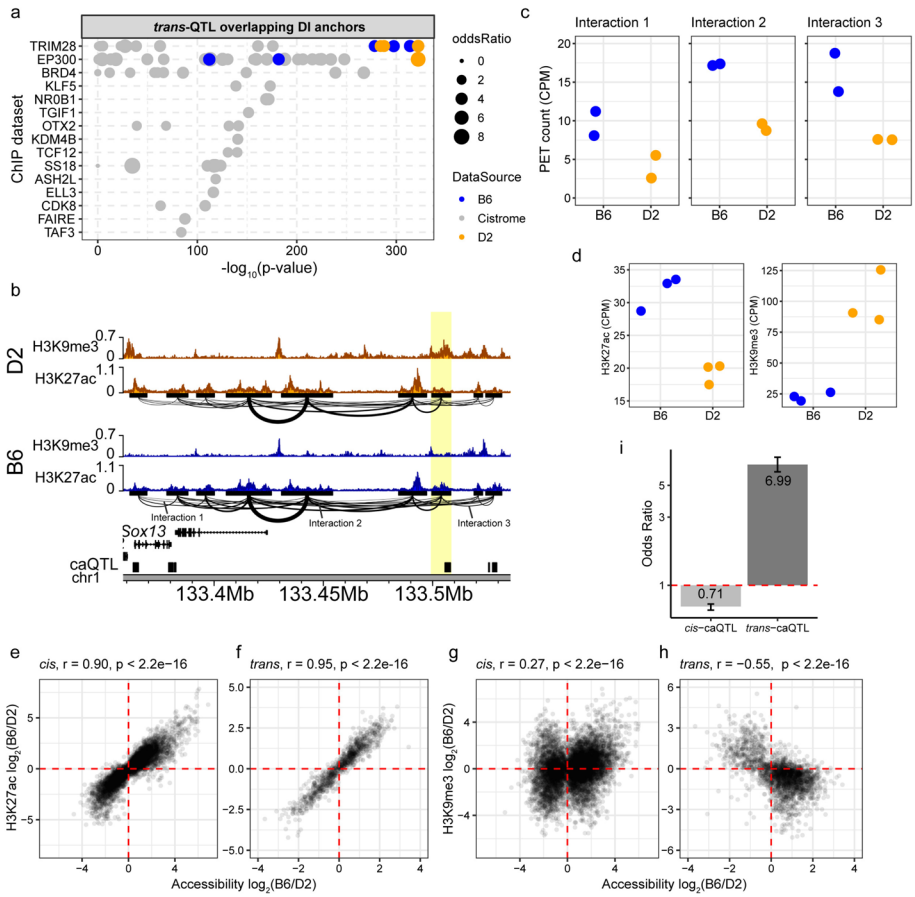

Fig. 3 Heterochromatin formation distinguishes *trans* from *cis* regulatory mechanisms. **a** Enrichment of the top 15 DNA-binding proteins at *trans*-QTL targets overlapping DI anchors. Each dot represents a ChIP-seq experiment either from publicly available database (gray—cistrome), or our previously published B6 (blue) and D2 (orange) datasets. Binding sites were evaluated for overlap between *trans*-targets and DI contact anchors (Fisher's exact test, top 15 factors with q-value cutoff < 0.01). **b** Genome profiles for H3K27ac and H3K9me3 ChIP enrichment from D2 (orange) and B6 (blue) at *Sox13* locus. HiChIP interactions indicated below H3K27ac tracks. Highlight indicates a contact anchor that overlaps a *trans*-target (black box). **c** HiChIP PET counts for three significant DIs indicated in panel *b* (Interaction 1 $p = 9.53e\text{-}3$, Interaction 2 $p = 1.05e\text{-}2$, Interaction 3 $p = 3.04e\text{-}3$). **d** Difference in H3K27ac (left) and H3K9me3 (right) at caQTL target highlighted in panel *b* between B6 and D2 (H3K27ac $p = 2.24e\text{-}3$, H3K9me3 $p = 3.58e\text{-}3$). Correlation between fold change (B6/D2) in H3K27ac enrichment and chromatin accessibility at *cis*- (**e**, n = 5509) and *trans*-QTL targets (**f**, $n = 989$). Correlation between fold change in H3K9me3 enrichment and chromatin accessibility at *cis*- (**g**, $n = 7621$) and *trans*-QTL targets (**h**, $n = 2356$). **i** Odds ratio showing that *trans*-targets are 6.99 times more likely to show discordant chromatin states resulting in high H3K9me3 and low ATAC

overlapping DIs, we predicted H3K9me3 enrichment in the strain with weaker contacts and H3K27ac enrichment in the strain with stronger contacts. To test this, we performed H3K9me3 and H3K27ac ChIP-seq in three independently derived mESC lines from both parental strains (Additional file 1: Fig. S5). At a putative CRE downstream from *Sox13* (Fig. 3b, c, d), D2 shows weaker chromatin interactions than B6 and increased H3K9me3 compared to B6 at the anchor overlapping a *trans*-QTL target (Fig. 3b, yellow highlight). Conversely, the same *trans*-QTL target showed increased H3K27ac in B6 compared to D2.

To broadly capture this trend, we quantified the level of both H3K27ac and H3K9me3 at both *cis* and *trans*-QTL targets and correlated strain-specific changes in histone modifications with changes in chromatin accessibility (Fig. 3e, f, g, h). When considering H3K27ac, we identified a strong positive correlation at *cis*- (Pearson $r = 0.90$, $p < 2.2e\text{-}16$) and *trans*- ($r = 0.95$, $p < 2.2e\text{-}16$) caQTL hotspot targets, indicating that both signify active chromatin. The key distinction in chromatin state is with H3K9me3. Comparing the change in H3K9me3 to change in chromatin accessibility, *cis*-QTL targets show values distributed across all four quadrants, whereas *trans*-QTL targets show a distinct pattern of discordant changes — defined as opposing changes in accessibility and H3K9me3 enrichment (Fig. 3g, h). This is supported quantitatively: *cis*-QTL targets showed a modest positive correlation, while *trans*-QTL targets showed a strong negative correlation ($r = -0.55$, $p < 2.2e\text{-}16$). Furthermore, when *trans*-QTL targets are stratified by QTL hotspot, each hotspot independently shows discordant relationship between H3K9me3 and accessibility, highlighting the generalizability of the relationship (Additional file 1: Fig. S6a-h). Critically, the proportion of *trans*-QTL targets with discordant chromatin states increases with QTL confidence (93% discordant at LOD 8; Additional file 1: Fig. S6i). Finally, *trans*-QTL targets were significantly more likely than *cis*-targets to show discordant chromatin states (odds ratio = 6.99, $p < 2.2e\text{-}16$, logistic regression; Fig. 3i), establishing heterochromatin formation as a defining feature of *trans*-regulation in mESCs. Together, these data support a molecular model in which genetic variation in *trans*-acting factors determine the location of H3K9me3 deposition, restricting chromatin accessibility and weakening 3D contacts at *trans*-QTL targets.

Chr13 trans-QTL coordinates chromatin accessibility and gene expression in an allele-specific manner

To determine the effect of *trans*-regulation on coordinated chromatin regulation and gene expression, we focused on a compound *trans*-QTL on Chr 13 that regulated the expression of 59 genes (eGenes) and 2,033 putative CREs (*trans*-QTL targets) with LOD ≥ 5 [28]. Spatial coordination of *trans*-QTL targets and eGenes was assessed for proximity enrichment using a modified Region Associated Differentially expressed gene approach [67], testing whether chromatin accessibility peaks cluster near transcriptionally regulated genes. Chr13 *trans*-caQTL targets showed higher enrichment near Chr13 eGenes compared to all other *trans*-QTL eGenes (Fig. 4a), indicating distal *trans*-regulation drives coordinated changes in chromatin accessibility and gene expression at co-localized target loci. Critically, this spatial coordination was directionally concordant with QTL effects; chromatin peaks with higher accessibility associated with the B6 allele at the QTL are specifically enriched near eGenes with higher expression when the

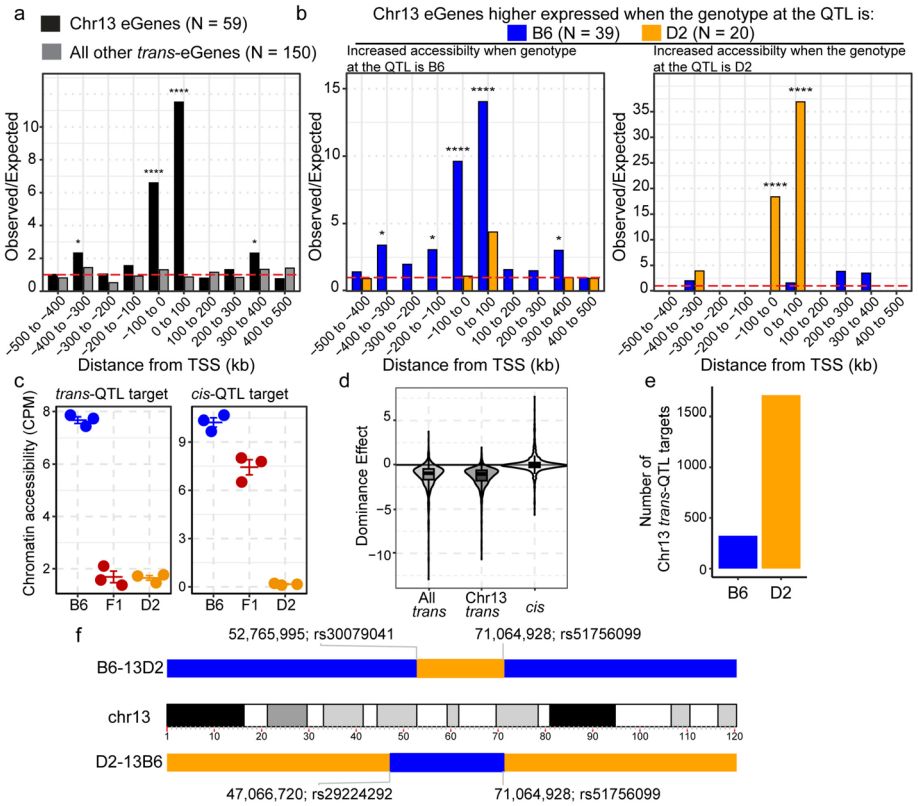

Fig. 4 Chr13 *trans*-QTL coordinates spatial regulation of chromatin accessibility and gene expression through dominant repression. **a** Observed-over-expected ratio for the spatial proximity between Chr13 *trans*-QTL targets to the transcription start sites (TSS) of either Chr13 eGenes (black) or all other *trans*-eGenes (gray). Red dashed line is null expectation (binomial test, * $p < 0.05$, ** $p < 0.01$, *** $p < 0.001$, **** $p < 0.0001$). **b** Similar to *a* except stratifying genes that are either higher expressed when Chr13 QTL haplotype is B6 (blue) or D2 (orange). Spatial proximity was tested for peaks with higher chromatin accessibility when Chr13 is B6 (left) or D2 (right). **c** Scatterplot of chromatin accessibility based on B6, D2, or F1-hybrid genotype of ESCs at two caQTL. Left – representative Chr13 *trans*-QTL target (Chr14:122,776,397) indicating dominant repressive effect on chromatin accessibility. Right – *cis*-QTL target (Chr5:104,727,903) representative of additive effect (line – mean, bars – standard error). **d** Distribution of dominance effect values in all *trans*-targets ($N = 836$), Chr13 *trans*-caQTL targets ($N = 575$), and all *cis*-caQTL targets ($N = 7049$). Negative values indicate repressive effect; values near zero indicate additive effect. **e** Classification of Chr13 *trans*-QTL targets by repressive allele. To establish directional predictions targets were stratified by which QTL genotype reduces chromatin accessibility, consistent with dominant repression. **f** Schematic of chromosome 13 showing the base-pair position and identifying SNP for congenic regions in B6-13D2 (D2 region on B6 background) and D2-13B6 (B6 region on D2 background) strains

genotype at the QTL is B6 (Fig. 4b, left), and the reciprocal pattern held for D2 (Fig. 4b, right). These analyses demonstrate that independently measured chromatin accessibility and gene expression are spatially coordinated by proximity in an allele-specific manner, supporting *cis*-propagation of *trans*-QTL through localized chromatin remodeling.

To determine the nature of the QTL effect on chromatin accessibility, we performed ATAC-seq on three independently derived mESCs from (B6xD2)F1 hybrids. Focusing on high-confidence caQTL (LOD > 8), *trans*-caQTL targets showed dominant repression, where F1 hybrid mESCs resembled the parent with lower accessibility. This is exemplified by the Chr13 *trans*-QTL target at Chr14:122,776,397, where the F1 showed the same low accessibility as the D2 parent (Fig. 4c, left). In contrast, a *cis*-QTL target at

Chr5:104,727,903 showed additive inheritance with F1 chromatin accessibility intermediate between the parent lines (Fig. 4c, right). To quantify this genome-wide, we calculated the dominance effect (d) as the deviation of F1 from the midparent value, where $d=0$ indicates additive inheritance and negative values indicate dominant repression [68]. This distinction between *trans* and *cis* effects extended genome-wide; *trans*-caQTL targets showed dominant repression (median $d=-0.95$), while *cis*-caQTL targets showed near-additive inheritance (median $d=-0.04$; Wilcoxon $p<2.2e-16$, effect size r = 0.61; Fig. 4d). Chr13 *trans*-caQTL targets specifically showed strong dominant repression (median $d=-1.04$), with the D2 allele at the Chr13 QTL associated with reduced accessibility at most targets (84%, $N=1,709$; Fig. 4e).

The dominant repressive inheritance pattern supports a model in which the Chr13 QTL encodes one or more diffusible repressors that establish heterochromatin at *trans*-QTL targets. To causally test whether this locus coordinates heterochromatin formation and 3D architecture, we generated reciprocal congenic mouse strains that exchange the Chr13 *trans*-QTL. The first strain, B6.D2-(rs30079041-rs51756099)/Bakr (hereafter referred to as B6-13D2), was bred to contain the D2 Chr13 congenic region (Chr13:52,765,995–71,064,928) on an otherwise B6 background. Conversely, D2.B6-(rs29224292-rs51756099)/Bakr (hereafter referred to as D2-13B6) was bred to carry the B6 Chr13 congenic region (Chr13:47,066,720–71,064,928) on an otherwise D2 background (Fig. 4f). Genome-wide SNP genotyping confirmed that congenic strains are inbred and genetically identical to their respective background strains except for the Chr 13 interval ("Methods" and Additional files 2, 3). Further, allele-specific gene expression analysis of mESCs derived from congenic mice provided additional validation (see below; Additional file 1: Fig. S7). Together, these congenic stem cells allow direct testing of predicted Chr13 *trans*-QTL effects on heterochromatin formation at *trans*-QTL targets.

Congenic strains confirm Chr13 trans-QTL drives heterochromatin formation at trans-QTL targets

To test whether the Chr13 *trans*-QTL drives *trans*-regulation of heterochromatin, we tested predictions based on QTL effects of BXDs on reciprocal mESCs from congenic strains. If Chr13 is causal, swapping the QTL region should alter chromatin state according to the genotype introduced. Specifically, B6-13D2 should resemble D2 at *trans*-QTL targets, while D2-13B6 should resemble B6. We tested these predictions using H3K9me3 and H3K27ac ChIP-seq, and ATAC-seq in B6, D2, B6-13D2, and D2-13B6 mESCs (Additional file 1: Fig. S8).

If repression is mediated by H3K9me3-marked heterochromatin, we predicted *trans*-QTL targets should show increased H3K9me3 in B6-13D2 (with D2 Chr13) compared to B6. Strikingly, 77% of Chr13 *trans*-caQTL targets showed the predicted H3K9me3 increase in B6-13D2 (Fig. 5a left, g; exact binomial test $p<2.2e-16$). Reciprocally, 89% showed decreased H3K9me3 in D2-13B6 (with B6 Chr13) compared to D2 (Fig. 5b left, g; $p<2.2e-16$). Of the remaining targets (324 loci predicted to be repressed when the allele at the QTL is B6), 69% showed the inverse pattern where H3K9me3 increased in D2-13B6 and decreased in B6-13D2 (Fig. 5a right, b left, right, g). Consistent with H3K9me3-mediated repression, active chromatin marks showed the reciprocal pattern as predicted. Targets gaining H3K9me3 in B6-13D2 showed reduced chromatin accessibility (77% of predicted decreases validated; Fig. 5c right, g) and reduced H3K27ac (94%

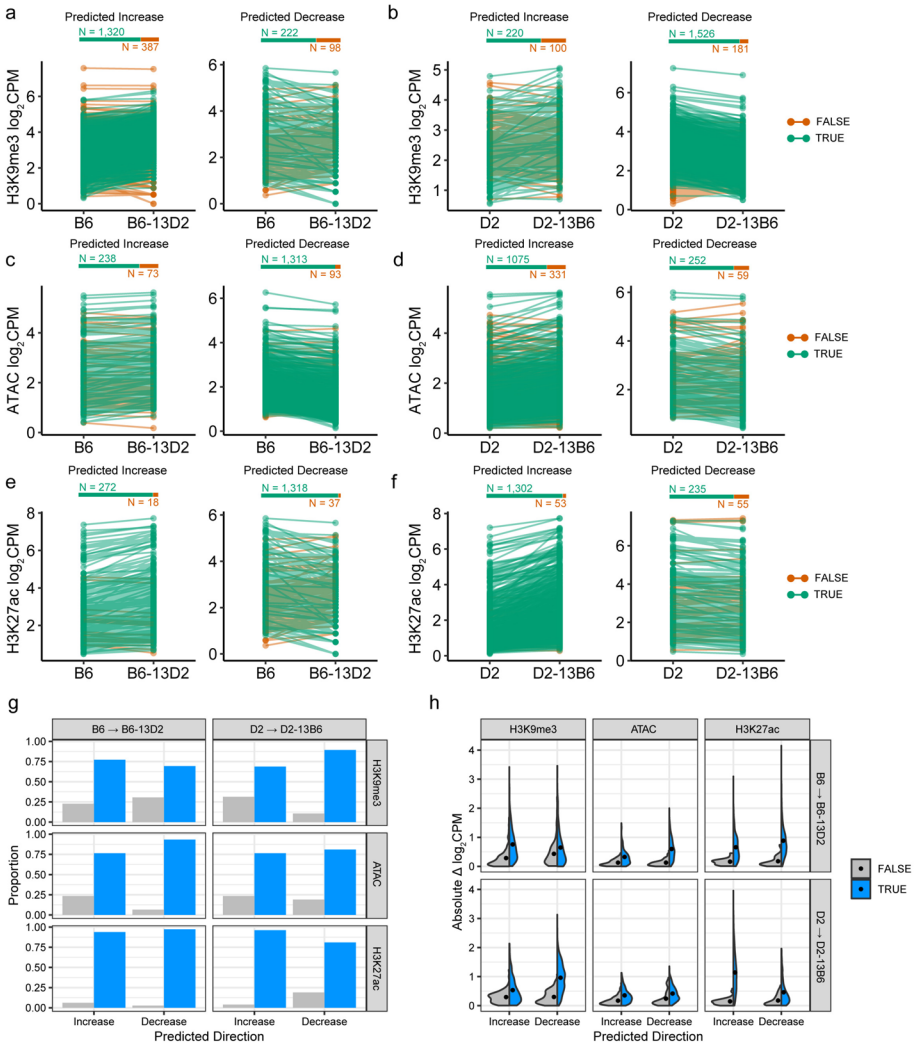

Fig. 5 Chr13 *trans*-QTL regulates heterochromatin formation at hundreds of distal loci. **a-f** Histone modification or chromatin accessibility at Chr13 *trans*-QTL targets in parental (B6 and D2) and reciprocal congenic (B6-13D2 and D2-13B6) strains for H3K9me3 ChIP-seq (**a**, **b**), ATAC-seq (**c**, **d**), and H3K27ac ChIP-seq (**e, f**). Each line represents a single *trans*-QTL target, connecting measurements between the parental strain (left) and its corresponding congenic (right). B6 → B6-13D2 panels (**a**, **c**, **e**) test the effect of introducing the D2 Chr13 region into the B6 background, while D2 → D2-13B6 panels (**b**, **d**, **f**) test the reciprocal introduction of the B6 Chr13 region into the D2 background. Within each panel, *trans*-QTL targets are separated by predicted direction of change based on QTL effect direction from BXD mapping: "Predicted Increase" (left) indicates targets expected to gain signal in the congenic strain, while "Predicted Decrease" (right) indicates targets expected to lose signal. Green lines indicate values that change in the predicted direction (true), while red lines indicate values that do not change in the predicted direction (false). Numbers above each plot show total *trans*-QTL targets tested that change as predicted (true = green) or do not change as predicted (false = red). Statistical significance assessed by exact binomial test. H3K9me3 enrichment: **a** increase $p < 2.2e\text{-}16$, decrease $p = 3.3e\text{-}12$; **b** increase $p = 1.7e\text{-}11$, decrease $p < 2.2e\text{-}16$ ATAC-seq: **c** increase $p < 2.2e\text{-}16$, decrease $p < 2.2e\text{-}16$; **d** increase $p < 2.2e\text{-}16$, decrease $p < 2.2e\text{-}16$. H3K27ac: **e** increase $p < 2.2e\text{-}16$, decrease $p < 2.2e\text{-}16$; **f** increase $p < 2.2e\text{-}16$, decrease $p < 2.2e\text{-}16$. **g** Observed proportion of Chr13 *trans*-QTL targets for which chromatin state changes in the direction predicted (i.e., true) based on QTL effect and dominant repression. **h** Violin plot showing distribution of absolute changes in $\log_2$ counts per million ($\log_2$CPM) at Chr13 *trans*-QTL targets. *Trans*-QTL targets that change as predicted (blue) or do not change as predicted (gray). Dots indicated median value

validated; Fig. 5e right, g). Similarly, *trans*-QTL targets losing H3K9me3 in D2-13B6 gained accessibility and H3K27ac (Fig. 5d left, f left, g). Further, *trans*-QTL targets that changed in the predicted direction showed significantly larger effect sizes than those that did not (Fig. 5h), indicating non-validated targets likely reflect measurement noise rather than biological exceptions. These reciprocal epigenomic changes, validated through two independent genetic perturbations across three chromatin features, directly demonstrate that Chr13 causally regulates hundreds of distal *trans*-QTL targets through heterochromatin formation.

Heterochromatin formation alters 3D contacts at trans-QTL target sites

To validate that Chr13-driven heterochromatin formation alters 3D interactions at *trans*-QTL targets, we repeated H3K27ac HiChIP in B6 and D2, while including B6-13D2 and D2-13B6 mESCs (two technical replicates per strain; Additional file 1: Fig. S9). We hypothesized that introducing the D2 Chr13 region in B6-13D2 would reduce chromatin interactions at *trans*-QTL targets (compared to B6), by increasing heterochromatin. Further, introducing the B6 Chr13 region into D2-13B6 would strengthen interactions (compared to D2), by reducing heterochromatin. Consistent with our hypothesis, at the *Litaf* locus we observed increased interactions in D2-13B6 compared to D2 (Fig. 6a, b, Interactions 1 and 2 $p < 0.027$). Reciprocally, at the same locus we observe weaker interactions in B6-13D2 compared to B6 (Fig. 6a, b; Interactions 1 and 2, $p < 1.51\text{e-}3$). This is particularly noteworthy because *Litaf* is a Chr13 *trans*-eQTL target, highlighting a potential functional link between chromatin architecture and gene regulation.

To test if heterochromatin formation underlies these changes in chromatin interactions, we examined H3K9me3 enrichment at the interaction anchors. Critically, H3K9me3 showed the reciprocal pattern to 3D contacts. At *Litaf*, D2-13B6 exhibited significantly lower H3K9me3 than D2 at the Chr13 *trans*-QTL target; and B6-13D2 showed increased H3K9me3 compared to B6 (Fig. 6c; DD13B $p = 4.81\text{e-}8$, BB13D $p = 2.98\text{e-}15$). These examples demonstrate that the Chr13 QTL drives heterochromatin formation at interaction anchors, coincident with altered 3D interaction strength. Further, in agreement with a heterochromatin-mediated mechanism, H3K27ac showed the opposite patterns, with D2-13B6 exhibiting higher levels at the same anchor compared to D2 at *Litaf* (Fig. 6d; $p < 9.24\text{–}103$), while B6-13D2 showed lower H3K27ac than B6 (Fig. 6d; $p = 4.54\text{e-}119$). Consistent DI patterns and opposing H3K9me3/H3K27ac profiles are observed at additional *trans*-QTL targets, including *Zfp516* and *Fam241a* (Additional file 1: Figs. S10-S11). Together these data confirm that Chr13 regulates heterochromatin formation and 3D organization at these *trans*-QTL targets.

To assess whether these examples reflect genome-wide patterns, we determined whether genetic differences in 3D contacts identified between parental strains (B6 and D2) predict changes in congenic strains. Remarkably, 73–83% of differential interactions changed in the predicted direction (Fig. 7a, b, Additional file 1: Fig. S12a; exact binomial test: all $p < 1.5\text{e-}8$). Furthermore, interactions that change contact frequency as predicted showed larger effect sizes than those that did not (Additional file 1: Fig. S12b).

To determine whether these changes in chromatin state and 3D contacts correspond to altered transcription, we performed RNA-seq on parent and congenic mESCs.

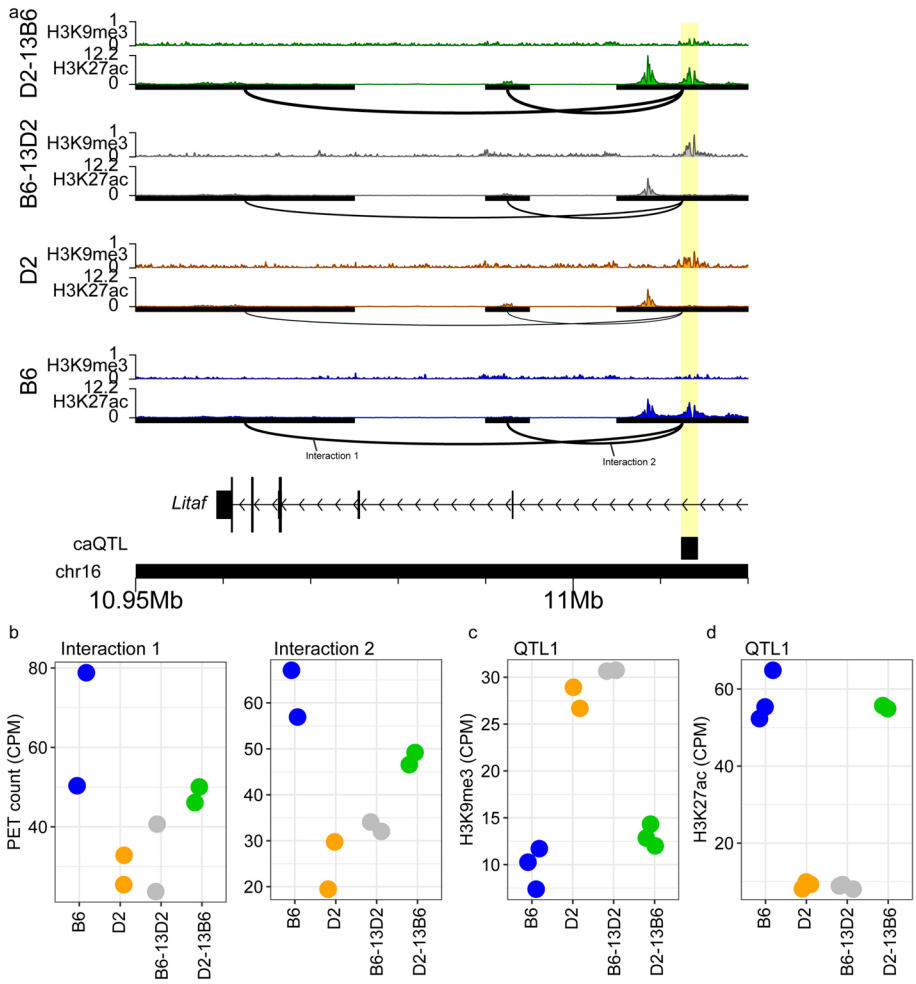

Fig. 6 Chr13 coordinates heterochromatin and 3D architecture at *Litaf* locus. **a** Genome profiles for H3K27ac and H3K9me3 ChIP enrichment from B6 (blue), D2 (orange), B6-13D2 (gray) and D2-13B6 (green) at the *Litaf* locus. HiChIP interactions indicated below H3K27ac tracks with the thickness of the arc connecting two anchors representing contact frequency. Highlight indicates a *trans*-QTL target (black box) overlapping a contact anchor and variable histone modifications. **b** HiChIP PET counts for all four strains for two interactions indicated in panel a (Interaction 1: BD $p = 4.67e\text{-}4$, BB13D $p = 3.14e\text{-}4$, DD13B $p = 2.68e\text{-}2$; Interaction 2: BD $p = 9.94e\text{-}5$, BB13D $p = 1.51e\text{-}3$, DD13B $p = 3.15e\text{-}3$). **c** H3K9me3 enrichment at Chr13 *trans*-QTL target highlighted panel a (BD $p = 8.25e\text{-}12$, BB13D $p = 2.98e\text{-}15$, DD13B $p = 4.81e\text{-}8$). **d** H3K27ac enrichment at Chr13 *trans*-caQTL target highlighted panel a (BD $p = 6.62e\text{-}108$, BB13D $p = 4.54e\text{-}119$, DD13B $p = 9.24e\text{-}103$). BD is the comparison between B6 and D2; BB13D is the comparison between B6 and B6-13D2; DD13B is the comparison between D2 and D2-13B6

Consistent with the chromatin data, 72–81% of Chr13 *trans*-eQTL targets changed in the predicted direction (Fig. 7c, d, Additional file 1: Fig. S12c), with validated genes showing larger effect sizes (Additional file 1: Fig. S12d). These validation rates, achieved across two independent genetic perturbations and testing reciprocal predictions, demonstrate that Chr13 causally regulates chromatin state at hundreds of distal loci with subsequent changes in nearby gene expression. The consistent validation across H3K9me3, H3K27ac, chromatin accessibility, 3D contact frequency, and gene expression establishes *trans*-regulation of heterochromatin as a mechanism for coordinated regulation of the epigenome (Fig. 7e).

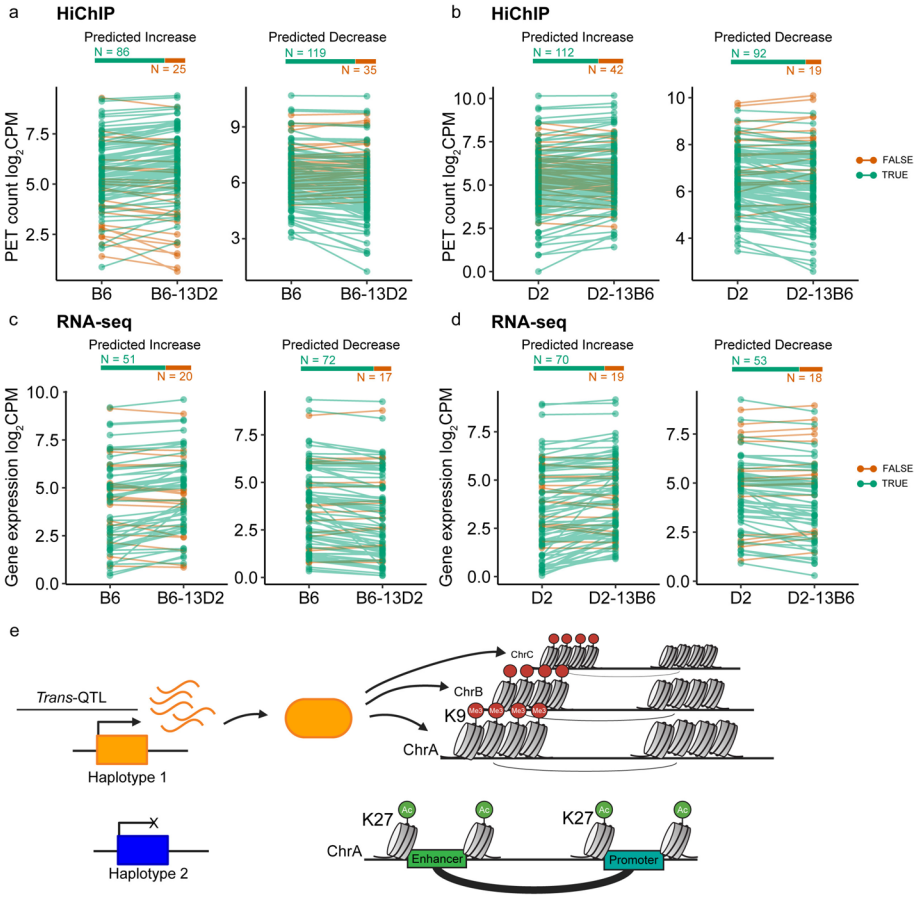

Fig. 7 Heterochromatin coordinates genome-wide changes in 3D architecture and gene expression. Validation of predicted changes in 3D contact frequency at Chr13 *trans*-QTL targets using H3K27ac HiChIP (**a**, **b**) or predicted changes in gene expression at Chr13 *trans*-eQTL targets using RNA-seq (**c**, **d**). Experimental design and visualization as in Fig. 5a-f, with each line representing a single interaction overlapping a Chr13 *trans*-QTL target: B6→B6-13D2 (**a**) and D2→D2-13B6 (**b**) or a single Chr13 eGene: B6→B6-13D2 (**c**) and D2→D2-13B6 (**d**). QTL targets were split by predicted direction of change based on BXD QTL mapping. Green lines indicate PET counts that change in the predicted direction (true); red lines indicate PET counts that do not change in the predicted direction (false). Numbers above show total interactions tested that are true (green) or false (red). Exact binomial test: **a** increase $p = 5.03e\text{-}9$, decrease $p = 6.59e\text{-}12$; **b** increase $p = 1.53e\text{-}8$, decrease $p = 1.12e\text{-}12$; **c** increase $p = 3.03e\text{-}4$, decrease $p = 3.17e\text{-}9$; **d** increase $p = 4.96e\text{-}8$, decrease $p = 3.89e\text{-}5$. **e** Model illustrating *trans*-regulation through heterochromatin formation. In this example, the orange haplotype *encodes* diffusible repressor(s) that establish H3K9me3-marked heterochromatin at distal *trans*-QTL targets (ChrA, B, C), reducing chromatin accessibility and weakening 3D contacts. Whereas the blue haplotype lacks active repressor(s), permitting open chromatin and stronger enhancer-promoter interactions and gene expression at the same distal locus

Discussion

Here, we establish heterochromatin formation as a molecular mechanism distinguishing *trans* from *cis* regulatory effects on genome organization in mESCs. *Trans*-QTL targets of the genome show a 6.99-fold enrichment for discordant H3K9me3 and chromatin accessibility, providing a unique epigenetic signature compared to *cis*-QTL targets. This mechanism is supported genetically by the dominant repressive pattern observed in F1 hybrids. Critically, reciprocal genetic perturbations demonstrated that a single locus causally coordinates distal chromatin state at hundreds of CREs with high concordance across molecular assays. Validation rates ranged from 73–83% for 3D contact frequency

to 89–94% for H3K9me3 and H3K27ac, demonstrating that the coordinated mechanism is robust across the epigenome. Together, these findings explain how *trans*-acting genetic variation achieves coordinated regulation across molecular layers through targeted heterochromatin deposition.

An important consideration in interpreting these results is that H3K27ac HiChIP measures contacts at H3K27ac-marked regions; differential signal may therefore reflect changes in contact frequency, histone modification, or both. Several studies have examined this using orthogonal approaches, finding that changes in 3D contacts and H3K27ac levels are correlated, suggesting coupled regulation. First, cell-type-specific interactions identified by H3K27ac HiChIP show significantly stronger signal in Hi-C from the corresponding cell type, confirming that differential HiChIP signal reflects true topological differences [69]. Second, when Hi-C and H3K27ac ChIP-seq are performed independently, genetic variation affecting interaction strength correlates with variation in H3K27ac levels, demonstrating that detection of this coordinated regulation is independent of enrichment-based methods [70]. Third, among differential interactions detected by ultra-deep Hi-C during cellular differentiation, H3K27ac increased nearly 14-fold at gained interaction anchors, while canonical interaction mediators CTCF and RAD21 increased only ~ 1.25-fold, indicating H3K27ac may determine relative interaction strength across conditions [71]. These findings support that interaction strength and H3K27ac enrichment are biologically coupled. Our *trans*-regulatory model predicts that heterochromatin formation coordinately restricts both H3K27ac and 3D contacts; correlation between these features is therefore the expected biological outcome.

Consistent with previous observations [60, 62, 72, 73], we find that 3D genome interactions are positively correlated with gene expression and active histone modifications, with contact frequency at individual loci associated with increased transcription. Prior work in human induced pluripotent stem cells (iPSCs) demonstrated that genetic variation affecting contact propensity results in coordinated changes in H3K27ac [70]; however, this study did not distinguish *cis* from *trans* regulation. Our findings extend beyond correlations by establishing causal relationships through reciprocal genetic perturbations and identifying heterochromatin formation as a defining feature of *trans*-regulation. Notably, the 20–25% of cases where increased contacts did not correspond to increased expression suggest additional regulatory mechanisms beyond direct connection between contact frequency and expression and warrant future investigation.

The functional genomic, genetic, and positional evidence support our leading hypothesis that the causal factors behind *trans*-regulation of heterochromatin is variation in genes that encode KRAB Zinc-Finger Proteins (KZFPs). Firstly, KZFPs provide DNA-binding specificity to recruit TRIM28, and chromatin modifying enzymes, to form heterochromatin [65, 74–78]. Consistent with this, TRIM28 is enriched at *trans*-QTL targets and a cluster of KZFPs is found in the Chr13 QTL [79]. Second, the unique association of *trans*-QTL targets with H3K9me3 and their dominant repressive effect in F1 hybrids indicates a diffusible silencing factor [27, 28]. Third, KZFPs are highly variable within species, indicating a source of rapid genetic variation [79, 80]. The Chr13 region represents a compound QTL containing structurally variant KZFP genes, each encoding distinct DNA-binding specificities; this genetic architecture explains how a single locus coordinates changes at hundreds of *trans*-QTL targets. Fourth, KZFPs have been

demonstrated to impact transcriptional repression through heterochromatin spreading from their DNA binding sites [81], supporting the regional *cis*-acting effects we see on enhancer-promoter contacts. Lastly, the epigenetic engineering approach of CRISPR interference (CRISPRi) [82] leverages a nuclease-dead Cas9 fused to a KRAB domain to induce heterochromatin and silence target genomic loci, directly demonstrating *trans*-regulation of heterochromatin. Building on this, recent work used CRISPRi to show that targeted H3K9me3 deposition led to a reduction in 3D contacts between enhancers and promoters [72], demonstrating direct effect of heterochromatin on 3D contacts in an inducible system.

We propose that *trans*-regulation of heterochromatin formation represents an evolutionarily advantageous mechanism for generating regulatory variation without disrupting core transcription factor (TF) networks. Classical models of *trans*-regulation invoke changes in TF expression or sequence, which would coordinately affect all targets genome-wide. However, developmental TFs and their core gene regulatory networks are under strong purifying selection due to their essential roles in lineage specification; and large variation in these factors likely results in severe phenotypic consequences. In contrast, KZFP DNA-binding domains evolve rapidly through structural variation [80, 83], and specifically at chromosome 13 in mice [79], potentially enabling population-level variation in which genomic regions are differentially targeted for heterochromatin formation based on the repertoire of zinc-finger domains present in an individual. Recent cross-species comparisons between human and macaque cells demonstrate that *trans*-regulatory divergence is specifically enriched at transposable elements bearing KZFP footprints [84], providing evolutionary support that heterochromatin variation drives regulatory divergence between populations while preserving core developmental networks. Further, heterochromatin acts as a barrier to pioneer transcription factor binding during cellular reprogramming [85, 86], and depletion of a specific KZFP reduced this barrier and enhanced reprograming efficiency [87]. The coordinated regulation we observe here reveals a potentially powerful and underappreciated layer of genome control where a single locus affects heterochromatin deposition and therefore chromatin accessibility, 3D contacts, and gene expression at hundreds of CREs. By allowing population-level variation in heterochromatin targeting rather than disrupting essential TF function, this proposed mechanism could provide standing regulatory variation necessary for evolutionary adaptation while maintaining developmental robustness.

The developmental implications of heterochromatin-mediated *trans*-regulation established in early pluripotency may extend to adult phenotypes. Heterochromatin can act as a barrier to lineage specification [85]; and variation in early heterochromatin formation may be propagated, creating a persistent epigenetic state that influences lineage commitment and cellular function. Supporting functional consequences, the Chr13 region investigated here has been associated with multiple developmental phenotypes in mice including craniofacial development, limb malformation, lupus susceptibility, meiotic recombination frequency, and imprint stability [27, 29–33]. The mechanism proposed here in mouse ESCs appears conserved in human biology. Kim et al. found that human KZFPs were enriched in donor-specific expression signatures across human iPSC lines [88]. They also observed reciprocal H3K9me3 patterning, where genes highly expressed in one line showed H3K9me3 enrichment in the other, mirroring the discordant

chromatin signature we identify at *trans*-QTL targets. This inter-individual variation in heterochromatin predicted differentiation propensity toward forebrain versus hindbrain fates, consistent with the model that heterochromatin variation creates tunable barriers affecting lineage-specific TF access. Further, KZFPs show dynamic expression beyond pluripotency, specifically upregulated in adult immune cells and neurons [83]. Consistent with functional relevance, genomic regions containing KZFPs in humans contain signatures of recent selection and are associated with adult disease [89]. Together, these observations suggest a model where early variation in heterochromatin establishment may constrain developmental outcomes and contribute to phenotypic variation in complex traits.

Our study provides genetic and epigenetic evidence that heterochromatin formation mediates *trans*-regulation of 3D genome organization and chromatin state in embryonic stem cells, but several limitations remain. First, all experiments were performed in mouse ESCs, and whether similar mechanisms operate in differentiated tissues, other species, or in vivo is unknown. However, our prior work identified similar epigenetic *trans*-regulation in male germ cells, hepatocytes, and cardiomyocytes [27]. Second, the Chr13 congenic interval spans a large region, making it unclear whether *trans*-regulation reflects the combined effects of this region or a single causal gene. Targeted perturbations, such as overexpression or CRISPR-based manipulation, will be needed to identify the causal gene(s). Finally, while reciprocal congenic experiments validate chromatin changes, functional consequences for pluripotency, lineage specification, and organismal phenotypes remain to be tested; and extension to human systems will be essential to establish relevance to complex traits and disease.

Conclusions

We establish heterochromatin formation as a defining chromatin signature distinguishing *trans* from *cis* regulatory mechanisms in mouse embryonic stem cells. Through reciprocal genetic perturbations, we demonstrate that genetic variation at a single *trans*-acting locus regulates chromatin accessibility, histone modifications, and 3D interactions at hundreds of distal regulatory elements, with coordinated effects on gene expression. This work provides a framework for understanding how *trans*-regulation operates mechanistically through targeted heterochromatin formation and suggests that genetic variation in early developmental chromatin states may contribute to phenotypic diversity in complex traits and disease susceptibility.

Methods

Mice

All mice were obtained from The Jackson Laboratory (Bar Harbor, ME) including C57BL/6J (JR# 000664) and DBA/2J (JR# 000671) parental inbred strains. To generate reciprocal congenic lines, B6 and D2 parents were intercrossed through F3, followed by marker-based genotyping and subsequent backcrossing for a minimum of 10 generations to generate the B6.D2-(rs30079041-rs51756099)/Bakr (JR# 37111) and D2.B6-(rs29224292-rs51756099)/Bakr (JR# 37112) congenic lines. Marker-based haplotype-specific PCR genotyping was performed using fluorescent KASP™ (LGC Genomics) genotyping reagents (variant Mb position, rs identifier, and primer

sequences are available in Additional file 4: Table S3). Ten generations of backcrossing is predicted to result in 0.049% residual donor genome, or approximately 1.3 Mb on average. Congenic genotyping and inbred status was confirmed using MiniMUGA array [90] (Neogen), which contains 2,903 informative markers between B6 and D2 backgrounds (~ 1 marker/Mb). The background analysis algorithm requires ≥ 2 concordant markers per 2 Mb to identify donor segments, providing > 90% power to detect regions exceeding 4 Mb. Reports for representative mice from each congenic line, confirmed homozygous for the congenic region by KASP assay, showed the expected donor contribution exclusively at the Chr 13 interval, with no evidence of residual donor genome elsewhere and 100% inbreeding (B6-13D2: Additional file 2; D2-13B6: Additional file 3). All animal experiments were approved by the Animal Care and Use Committee of The Jackson Laboratory (Summary #16043). Congenic lines are available upon request.

Derivation and maintenance of mouse embryonic stem cells

All mouse ESCs used in this study were derived in house from the following genetic backgrounds: B6, D2, (B6xD2)F1 hybrids, and B6-13D2 and D2-13B6 congenic lines. Derivation of the B6, D2, and F1 ESCs were previously described in Byers et al. [28]. Derivation of embryonic stem cells for B6-13D2 and D2-13B6 congenic strains were performed using the protocol outlined in Czechanski et al. [91]. Authentication of B6-13D2 and D2-13B6 congenic intervals within the ESCs was performed by using fluorescent KASP™ (LGC Genomics) assay similar to the respective mouse strains, and sex was verified using *Sry* specific primers. Additional information regarding primer sequences and genomic locations is provided in Additional file 4: Table S3. All cell lines tested negative for mycoplasma contamination and are available upon request. For all cultures, mouse ESCs were seeded with irradiated mouse embryonic fibroblasts (MEFs) from B6 animals and cultured in DMEM high glucose base medium supplemented with 15% fetal bovine serum (FBS, Lonza, cat. no. 14-501F lot no. 0000217266), 1X Pen/Strep, 2 mM GlutaMAX, 1 mM sodium pyruvate, 0.1 mM MEM-NEAA, 0.1 mM 2-mercaptoethanol, 103 IU LIF, 1 μM PD0325901, and 3 μM CHIR99021. Mouse ESCs were expanded for 2–3 days to reach ~ 70% confluency for molecular assays. For functional genomic assays, mouse ESCs were enzymatically disassociated into single cell suspensions using trypsin and MEFs were depleted by incubation on gelatine coated plates for 20 min.

ATAC-seq sample preparation and sequencing

ATAC-seq experiments were performed, using two or three independent cultures from the same cell line per strain, following the FAST-ATAC method as described [92], using 100,000 cells. DNA quality and quantity was determined using High Sensitivity D5000 ScreenTape (Agilent Technologies). Libraries were sequenced to a read depth of about 40 million reads per sample on an Illumina NovaSeq X Plus with a 150 bp read length.

Chromatin Immunoprecipitation (ChIP) sample preparation and sequencing

ChIP-seq experiments performed with B6 and D2 used three independently derived cell lines from each strain. Validation ChIP-seq experiments performed with B6, D2, B6-13D2, and D2-13B6 used two or three independent cultures from the same cell line for each strain. For each ESC ChIP-seq library, 3 million cells were harvested and fixed as previously described [27]. Cell lysis, chromatin fragmentation, and immuno- precipitation were performed as described [93], with minor modifications. For H3K27ac ChIP, sodium butyrate was added to hypotonic lysis buffer, MNase buffer, RIPA buffer (post-overnight antibody conjugation), RIPA wash buffer, and TE to inhibit histone deacetylase activity. Immunoprecipitation was performed using antibodies against H3K27ac (12 µL, abcam, ab4729, lot# GR312658-1; Cell Signaling Technology, 8173, lot# 9) and H3K9me3 (6 µL, Active Motif, 39,161, lot# 09919003). ChIP-seq libraries were constructed using the KAPA HyperPrep Kit (Roche Sequencing and Life Science). Quality and concentration of libraries were assessed using the High Sensitivity D5000 ScreenTape (Agilent Technologies) and KAPA Library Quantification Kit (Roche Sequencing and Life Sciences). Libraries were sequenced to a read depth of about 40 million reads per sample (75 bp) on an Illumina NextSeq or NovaSeq X Plus.

RNA-seq sample preparation and sequencing

RNA-seq experiments performed with B6, D2, B6-13D2, and D2-13B6 used three independent cultures from the same cell line for each strain, with the exception of B6 (two independent cultures from the same cell line and one culture from an independently derived cell line from the same strain). For each library, 1 million cells were collected, and RNA was isolated using the NucleoMag RNA Kit (Machery-Nagel) and the KingFisher Flex purification system (ThermoFisher). RNA concentration and quality were assessed using the Nanodrop 8000 spectrophotometer (Thermo Scientific) and the RNA ScreenTape (Agilent Technologies). Libraries were constructed using the mRNA Library Prep Kit (Watchmaker) and assessed using the D5000 ScreenTape (Agilent Technologies) and Qubit dsDNA HS Assay (ThermoFisher), respectively. Libraries were sequenced 150 bp paired-end on an Illumina NovaSeq X Plus to a read depth of about 40 million reads per sample.

HiChIP sample preparation and sequencing

Restriction enzyme based HiChIP

HiChIP experiments were performed as described [39], using two samples from independently derived cell lines per strain. We used 10 million cells, DpnII (NEB, R05443), and the following 3C modifications [94] to improve digestion, incorporation, ligation, and removal of dangling ends. Specifically, 1) biotin incorporation was performed at 23 °C for 4 h with interval shaking (10 s at 900 rpm, 5 min off). 2) Ligation was performed at 16 °C for 4 h with interval shaking (1 min at 500 rpm, 4 min off). 3) Samples were sheared using a Diagenode Biorupter with the following parameters: tube size = 1.5 mL, time on = 30 s, time off = 30 s, cycle # = 8. 4) A total of 3 µL of H3K27ac antibody (Abcam #ab4729) was added to the sample and incubated at 4 °C overnight with rotation. 5) After ChIP washes, samples were resuspended in 20 µL removal of biotin-dATP master mix: 5 µL 10X NEB Buffer 2.1, 0.125 µL of dATP and dGTP at 10 mM

each, 5 µL T4 DNA polymerase (NEB, M0203), and 39.8 µL distilled water. Samples were incubated at 20 °C for 4 h with interval shaking (1 min at 400 rpm, 4 min off). Lastly, size selection of libraries was performed using a two-sided selection with AMPureXP beads. Briefly, 22.5 µL of beads were added to the sample to capture fragments less than 700 bp. Supernatant was transferred to a new tube and 13.5 µL of beads were added to the supernatant sample to capture fragments greater than 300 bp. Libraries were eluted in 50 µL 10 mM Tris pH 8.0. Libraries were quantified using qPCR against Illumina primers and then paired end sequenced with read length of 75 bp to a sequencing depth of 200 million reads per sample over two Illumina NextSeq runs.

Dovetail HiChIP MNase Kit

The Dovetail HiChIP MNase Kit was used for HiChIP for validation experiments repeating B6, D2, and including B6-13D2 and D2-13B6. HiChIP was performed using two samples from independent cultures from the same cell line per strain. The User Guide [95] (version 2.0) was used to process samples of 10 million cells. H3K27ac (Cell Signaling Technology, 8173, lot #9) was used for immunoprecipitation. Libraries were assessed using the D5000 ScreenTape (Agilent Technologies) and Qubit dsDNA HS Assay (ThermoFisher), respectively. Libraries were paired end sequenced with a read length of 150 bp to a sequencing depth of 300 million reads per sample (over two flow cell lanes) on an Illumina NovaSeq X Plus.

ATAC-seq and ChIP-seq data processing

Illumina adaptors were trimmed from ChIP reads using Trimmomatic [96] (version 0.39) and then aligned to mouse reference genome (mm10), modified to incorporate known D2 variants reported in Mouse Genomes Project Database, REL-1505 [26, 97] using hisat2 [98] (version 2.2.1). Duplicate reads were removed using Picard Tools [99] (version 2.0.1), and peaks were called for each sample using MACS [100] (version 1.4.2). While independent peak calling was performed on H3K27ac and H3K9me3 to determine quality and reproducibility, to compare ATAC- and ChIP-seq signal at QTL targets the comprehensive set of open chromatin locations (i.e., peakome) previously developed [28] was used to generate read counts across all samples using bedtools [101] (version 2.9.2) similar to ATAC-seq. Read matrices were TMM-normalized and $\log_2$-transformed downstream differential analysis of histone modification using edgeR [102] (version 3.34.1). For visualization on genome browser tracks with karyoploteR [103] (version 1.20.3) we used bwa [104] (version 0.7.5; filter mapping quality < 30, unmapped, secondary, QC fail, duplicates, and supplementary reads) alignment to generate bigwig files.

Dominance effects were calculated following Tian et al. [68]. BXD recombinant inbred lines are homozygous at all loci, so at each caQTL, lines carry either the B6/B6 or D2/D2 genotype. The dominance effect was estimated as the difference between the (B6/D2)F1 hybrid and the midparent value: $d = \mu\_BD - (\mu\_BB + \mu\_DD)/2$, where µ_BB and µ_DD represent mean chromatin accessibility at the target in BXD lines stratified by B6 or D2 genotype at the mapped QTL, and µ_BD is the F1 hybrid mean. Under this formulation, $d = 0$ indicates additive inheritance where heterozygotes are intermediate between homozygous means, negative values indicate dominant repression where heterozygotes resemble the lower-accessibility parent, and positive values indicate dominant activation

where heterozygotes resemble the higher-accessibility parent. Analyses were restricted to high-confidence caQTL (LOD ≥ 8).

RNA-seq data processing

Allele-specific expression was quantified using EMASE [105] (v0.10.16) to generate gene-level expression estimates for compatibility with previous eQTL analysis and validate congenic mESC genotypes. Single-end reads were aligned to a diploid B6 × D2 hybrid transcriptome constructed from Ensembl release 78 (R78-REL1505) using bowtie [106] (v1.0.0) with parameters: –best -a –strata -v 3 -m 100. Alignments were processed with EMASE model 4 to generate per-gene expected read counts each allele. B6/(B6 + D2) allele ratios were calculated per gene from transcript-per-million estimates. To identify genes where EMASE reliably distinguishes alleles, parental B6 and D2 samples served as truth sets; genes were retained where mean B6 parental ratio > 0.8 and mean D2 parental ratio fell < 0.4, yielding 2,863 informative genes (42 within the Chr13 congenic interval). For gene expression analysis in congenic and parental strains, EMASE total expected counts were TMM-normalized and $\log_2$-transformed downstream differential analysis using edgeR [102] (version 3.34.1).

HiChIP data processing and analysis

Restriction enzyme-based HiChIP

HiChIP reads were processed using HiC-Pro [107] (v2.11.4) with the following parameters:

```
N_CPU = 4, SORT_RAM = 768 M
REFERENCE_GENOME = mm10
LIGATION_SITE = GATCGATC
MIN_FRAG_SIZE = 30
MAX_FRAG_SIZE =100000
MIN_INSERT_SIZE = 30
MAX_INSERT_SIZE = 600
```

Long-range interactions were called with hichipper [108] (v.0.7.8b0) using H3K27ac ChIP-seq peaks generated in this paper. PET counts were imported into RStudio (version 4.1) using diffloop [109] (v1.22.0). Before filtering data, read matrices were TMM-normalized. Anchors of interactions were not merged and interactions less than 5,000 bp were filtered out. P-values were adjusted using an FDR cutoff of 0.01. Interactions were filtered for at least four read counts in at least two samples before identifying differential interactions using DESeq2 [110] within the diffloop [109] package. Significant differential interactions were cutoff at FDR ≤ 0.2. Differential interactions (DIs) showed higher average PET counts than non-differential interactions (Wilcoxon rank sum test $p < 2.2e\text{-}16$; Additional file 1: Fig. S13), consistent with increased statistical power to detect differences at well-covered loci. Interactions were annotated using the basic gene annotation from Gencode (Release M25) and the enhancer reference from ENCODE (ENCFF580RGZ, Release M21).

Dovetail HiChIP MNase Kit

HiChIP reads were processed using Dovetail's HiChIP Loop Calling [111] (readthedocs Revision 8f2e0b16). Reads were aligned to mm10 using bwa [104] (v0.7.18). pairtools [112] (version 1.1.2) was used to record and sort valid ligation events, remove PCR duplicates, and generate.pairs and bam files. Samtools [113] (version 1.19.2) was used to create and index the final bam file. Libraries were verified to have no-dup read pairs ≥ 50%, about 20% or greater of the total mapped non-dup pairs to be in *cis* and > 1 kb in length, and total reads in 1 kb around center of ChIP peaks > 2%. Filtered pairs were converted to Hi-C Pro valid pairs format. Loops were called using FitHiChIP [114] (version 11.0) with the following parameters in the bias correction/coverage bias configuration file:

Interaction type = peak to peak
Bin size = 2500
Lower distance threshold = 10,000
Upper distance threshold = 2,000,000
Bias types = coverages bias regression
Merge filtering was employed (option 1)
q-value = 0.01
Chromosome sizes correspond to mm10

Peak-to-peak interactions were imported into RStudio (version 4.1). diffloop [109] (version 1.22.0) was used to adjust p-values using an FDR cutoff of 0.01. Interactions were filtered for at least four read counts in at least two samples. PET counts were normalized, and edgeR [102] (version 3.34.1) was used to identify differential interactions (FDR < 0.2).

caQTL enrichment at differential interaction anchors

Enrichment of caQTL targets was assessed using the regioneR package [115] (version 1.26.1). Left and right anchors from differential interactions were randomized by circularizing chromosomes to preserve regional structure and maintaining the observed anchor and interaction widths. For each permutation, overlaps between randomized regions and caQTL targets were classified as overlaps with no anchors, one anchor, or both anchors. The permutation test was repeated 1,000 times, and enrichment was quantified using Z-score.

Spatial enrichment analysis

Region Associated Differentially expressed gene (RAD) framework [67] was adapted to test whether chromatin accessibility changes and gene expression changes regulated by the Chr13 *trans*-QTL spatially co-localize. The genomic background was defined as genes expressed in ESCs consistent with cutoff used for QTL mapping [28], rather than all annotated genes genome-wide. Strand-specific signed distances between each gene's TSS to nearby chromatin accessibility peaks were calculated, with negative values indicating peak positions upstream of the TSS in the direction of transcription and positive values indicating downstream positions. Distances were binned into 100 kb intervals spanning −500 kb to + 500 kb relative to the TSS. Binomial tests were used to determine

significance treating each gene-peak connection within 500 kb as an independent trial (binom.test in R, alternative = 'greater'), with the expected probability defined by the genome-wide proportion of focal genes (p = M_focal/N_total), and Benjamini–Hochberg correction was applied for multiple testing within each analysis.

3C-qPCR

3C-qPCR experiments were performed as previously described [64] with the following modifications. Briefly, 1) 10 million cells were fixed with fresh formaldehyde at a final concentration of 1% for 10 min with rotation before quenching the reaction with 10X glycine for 5 min with rotation. Cells were pelleted, washed with PBS, and flash frozen; 2) 800 U restriction enzyme (NEB, #R0101) and 1 mM ATP were used for digestion; 3) 4,000 U ligase (NEB, #M0202) was used for an overnight incubation at 16 °C; 4) Qiagen MaXtract HD tubes were used for 3C sample purification. To control for differential primer efficiency and establish a baseline for random ligation events, we generated control libraries from bacterial artificial chromosomes (BACs) spanning the interrogated loci (Additional file 4: Table S4). BAC DNA was digested with the same restriction enzyme and ligated, producing a template where all ligation products are present at equal concentrations independent of chromatin organization [64]. Interaction frequencies in 3C libraries were normalized to BAC control signals to account for primer pair efficiency and distinguish chromatin-mediated interactions from background. Primers used for 3C-qPCR experiments are listed in Additional file 4: Table S3.

Supplementary Information

The online version contains supplementary material available at https://doi.org/10.1186/s13059-026-04155-2.

Additional file 1: Supplementary figures S1-S13: Fig. S1. HiChIP differential interactions are enriched for caQTL targets. Fig. S2. 3C-qPCR validates stronger interactions in B6 at *Zfp951* locus. Fig. S3. 3C-qPCR validates stronger interactions in D2 at *Bicc1* locus. Fig. S4. 3C-qPCR validates stronger interactions in B6 at *Manbal* locus. Fig. S5. Quality control of ChIP-seq data reveals strong reproducibility among replicates. Fig. S6. H3K9me3 enrichment at *trans*-caQTL hotspot targets is negatively correlated with chromatin accessibility. Fig. S7. Allele-specific gene expression confirms congenic strain identity. Fig. S8. Quality control of ChIP-seq and ATAC-seq reveals strong reproducibility among replicates. Fig. S9. Quality control of HiChIP data reveals strong reproducibility among replicates. Fig. S10. Chr13 coordinates heterochromatin and 3D architecture at *Fam241a* locus. Fig. S11. Chr13 coordinates heterochromatin and 3D architecture at *Zfp516* locus. Fig. S12. Chr13 *trans*-QTL coordinates genome-wide changes in 3D genome contacts and gene expression. Fig. S13. Differential interactions show higher PET counts than non-differential interactions.

Additional file 2. B6-13D2 MiniMUGA genotyping results: Genotyping confirmation that the Chr13 congenic region from B6-13D2 is D2-derived on an otherwise B6-derived background.

Additional file 3. D2-13B6 MiniMUGA genotyping results: Genotyping confirmation that the Chr13 congenic region from D2-13B6 is B6-derived on an otherwise D2-derived background.

Additional file 4: Supplementary tables: Table S1. DIs at different FDRs. Table S2. Overlap and enrichment of caQTL targets at DI anchors. Table S3. All primers used for experiments. Table S4. Bacterial Artificial Chromosomesused as PCR controls for 3C-qPCR.

Acknowledgements

We would like to thank all the members of the Baker laboratory for comments and discussion. Additionally, we would like to thank Steve Munger for comments on the manuscript and Natalie Powers and Petko Petkov for their early breeding of the congenic lines. We recognize contributions from The Jackson Laboratory Genome Technologies services. The Jackson Laboratory scientific services are supported in part through the National Cancer Institute's Cancer Core Grant P30CA034196. We acknowledge BioRender for its illustration tools used to create Fig. 7e (https://BioRender.com/5ojnzqy).

Peer review information

Wenjing She was the primary editor of this article and managed its editorial process and peer review in collaboration with the rest of the editorial team. The peer-review history is available in the online version of this article.

Authors' contributions

CLB and HJF conceptualized the study and contributed to methodology. CLB provided resources. HJF, AZS, and AB investigated the study. HJF and CLB performed data curation and formal analysis. HJF and CLB performed visualization. HJF and CLB wrote the manuscript. HJF and CLB revised and edited the manuscript. CLB performed supervision. CLB performed funding acquisition. All authors read and approved the final manuscript.

Funding

This work was supported by the National Institute of General Medical Sciences (NIGMS) grant R35GM133724.

Data availability

Original data discussed in this study are available in the NCBI's Gene Expression Omnibus (GEO) through Series accession GSE312918 [116]. Processed data tables in the accession include read count matrices for ATAC-seq, H3K27ac ChIP-seq, H3K9me3 ChIP-seq, RNA-seq, and HiChIP. Additionally, bigwig files for each ATAC, ChIP, and HiChIP sample are provided for visualization. H3K4me3 ChIP-seq (GSE113192) [27, 117] and ATAC-seq and RNA-seq (GSE164935) [28, 118] for B6, D2 parental, and (B6xD2)F1 ESCs were collected previously and are available through GEO.

Declarations

Ethics approval and consent to participate

All animal procedures were approved by the Animal Care and Use Committee of The Jackson Laboratory under protocol number 04008.

Consent for publication

Not applicable.

Competing interests

The authors declare no competing interests.

Received: 10 December 2025 Accepted: 8 June 2026
Published online: 13 June 2026

References

1. Maurano MT, Humbert R, Rynes E, Thurman RE, Haugen E, Wang H, et al. Systematic Localization of Common Disease-Associated Variation in Regulatory DNA. Science. American Association for the. Adv Sci. 2012;337:1190–5. https://doi.org/10.1126/science.1222794.
2. Tak YG, Farnham PJ. Making sense of GWAS: using epigenomics and genome engineering to understand the functional relevance of SNPs in non-coding regions of the human genome. Epigenetics Chromatin. 2015;8:57. https://doi.org/10.1186/s13072-015-0050-4.
3. Ward LD, Kellis M. Evidence of abundant purifying selection in humans for recently-acquired regulatory functions. Science. 2012;337:1675–8. https://doi.org/10.1126/science.1225057.
4. Guan Y, Liu H, Ma Z, Li S-Y, Park J, Sheng X, et al. Dnmt3a and Dnmt3b-Decommissioned Fetal Enhancers are Linked to Kidney Disease. J Am Soc Nephrol. 2020;31:765–82. https://doi.org/10.1681/ASN.2019080797.
5. Ma Y, Buttitta L. Chromatin organization changes during the establishment and maintenance of the postmitotic state | Epigenetics & Chromatin | Full Text. Epigenetics & Chromatin. 2017;10. https://doi.org/10.1186/s13072-017-0159-8. Cited 2021 June 22.
6. Fagnocchi L, Cherubini A, Hatsuda H, Fasciani A, Mazzoleni S, Poli V, et al. A Myc-driven self-reinforcing regulatory network maintains mouse embryonic stem cell identity. Nat Commun. 2016;7:11903. https://doi.org/10.1038/ncomms11903.
7. Atlasi Y, Stunnenberg HG. The interplay of epigenetic marks during stem cell differentiation and development | Nature Reviews Genetics. Nat Rev Genet. 2017;18:643–58. https://doi.org/10.1038/nrg.2017.57.
8. Dixon JR, Jung I, Selvaraj S, Shen Y, Antosiewicz-Bourget JE, Lee AY, et al. Chromatin architecture reorganization during stem cell differentiation. Nature Nature Publishing Group. 2015;518:331–6. https://doi.org/10.1038/nature14222.
9. Javierre BM, Burren OS, Wilder SP, Kreuzhuber R, Hill SM, Sewitz S, et al. Lineage-Specific Genome Architecture Links Enhancers and Non-coding Disease Variants to Target Gene Promoters. Cell Elsevier. 2016;167:1369-1384.e19. https://doi.org/10.1016/j.cell.2016.09.037.
10. Zhang F, Lupski JR. Non-coding genetic variants in human disease. Hum Mol Genet. 2015;24:R102–10. https://doi.org/10.1093/hmg/ddv259.
11. Rockman MV, Kruglyak L. Genetics of global gene expression. Nat Rev Genet. 2006;7:862–72. https://doi.org/10.1038/nrg1964. Nature Publishing Group.
12. Liu X, Mefford JA, Dahl A, He Y, Subramaniam M, Battle A, et al. GBAT: a gene-based association test for robust detection of trans-gene regulation. Genome Biol. 2020;21:211. https://doi.org/10.1186/s13059-020-02120-1.
13. Mostafavi H, Spence JP, Naqvi S, Pritchard JK. Systematic differences in discovery of genetic effects on gene expression and complex traits. Nat Genet. 2023;55:1866–75. https://doi.org/10.1038/s41588-023-01529-1. Nature Publishing Group.
14. Tyler AL, Mahoney JM, Keller MP, Baker CN, Gaca M, Srivastava A, et al. Transcripts with high distal heritability mediate genetic effects on complex metabolic traits. Nat Commun. 2025;16:5507. https://doi.org/10.1038/s41467-025-61228-9. Nature Publishing Group.

15. Westra H-J, Peters MJ, Esko T, Yaghootkar H, Schurmann C, Kettunen J, et al. Systematic identification of trans eQTLs as putative drivers of known disease associations. Nat Genet. 2013;45:1238–43. https://doi.org/10.1038/ng.2756. Nature Publishing Group.
16. Wheeler HE, Ploch S, Barbeira AN, Bonazzola R, Andaleon A, Fotuhi Siahpirani A, et al. Imputed gene associations identify replicable trans-acting genes enriched in transcription pathways and complex traits. Genet Epidemiol. 2019;43:596–608. https://doi.org/10.1002/gepi.22205.
17. Yao DW, O'Connor LJ, Price AL, Gusev A. Quantifying genetic effects on disease mediated by assayed gene expression levels. Nat Genet. 2020;52:626–33. https://doi.org/10.1038/s41588-020-0625-2. Nature Publishing Group.
18. Albert FW, Bloom JS, Siegel J, Day L, Kruglyak L. Genetics of trans-regulatory variation in gene expression. eLife. 2018;7:e35471. https://doi.org/10.7554/eLife.35471.
19. Visscher PM, Wray NR, Zhang Q, Sklar P, McCarthy MI, Brown MA, et al. 10 Years of GWAS Discovery: Biology, Function, and Translation. Am J Hum Genet. 2017;101:5–22. https://doi.org/10.1016/j.ajhg.2017.06.005.
20. Cirulli ET, Goldstein DB. Uncovering the roles of rare variants in common disease through whole-genome sequencing. Nat Rev Genet. 2010;11:415–25. https://doi.org/10.1038/nrg2779. Nature Publishing Group.
21 Zuk O, Schaffner SF, Samocha K, Do R, Hechter E, Kathiresan S, et al. Searching for missing heritability: Designing rare variant association studies. Proc Natl Acad Sci. 2014;111:E455-64. https://doi.org/10.1073/pnas.1322563111.
22. Churchill GA, Gatti DM, Munger SC, Svenson KL. The Diversity Outbred Mouse Population. Mamm Genome. 2012;23:713–8. https://doi.org/10.1007/s00335-012-9414-2.
23. Svenson KL, Gatti DM, Valdar W, Welsh CE, Cheng R, Chesler EJ, et al. High-Resolution Genetic Mapping Using the Mouse Diversity Outbred Population. Genetics. 2012;190:437–47. https://doi.org/10.1534/genetics.111.132597.
24 Williams RW, Gu J, Qi S, Lu L. The genetic structure of recombinant inbred mice: High-resolution consensus maps for complex trait analysis. Genome Biol. 2001;2:preprint0007.1. https://doi.org/10.1186/gb-2001-2-8-preprint0007.
25. Taylor BA, Wnek C, Kotlus BS, Roemer N, MacTaggart T, Phillips SJ. Genotyping new BXD recombinant inbred mouse strains and comparison of BXD and consensus maps. Mamm Genome. 1999;10:335–48. https://doi.org/10.1007/s003359900998.
26. Keane TM, Goodstadt L, Danecek P, White MA, Wong K, Yalcin B, et al. Mouse genomic variation and its effect on phenotypes and gene regulation. Nature. 2011;477:289–94. https://doi.org/10.1038/nature10413.
27. Baker CL, Walker M, Arat S, Ananda G, Petkova P, Powers NR, et al. Tissue-Specific Trans Regulation of the Mouse Epigenome. Genetics. 2019;211:831–45. https://doi.org/10.1534/genetics.118.301697.
28. Byers C, Spruce C, Fortin HJ, Hartig EI, Czechanski A, Munger SC, et al. Genetic control of the pluripotency epigenome determines differentiation bias in mouse embryonic stem cells. Embo J. 2021;40:e109445. https://doi.org/10.15252/embj.2021109445. John Wiley & Sons, Ltd.
29. Johnson KR, Lane PW, Ward-Bailey P, Davisson MT. Mapping the mouse dactylaplasia mutation, Dac, and a gene that controls its expression, mdac. Genomics. 1995;29:457–64. https://doi.org/10.1006/geno.1995.9981.
30. Kano H, Kurahashi H, Toda T. Genetically regulated epigenetic transcriptional activation of retrotransposon insertion confers mouse dactylaplasia phenotype. Proc Natl Acad Sci U S A. 2007;104:19034–9. https://doi.org/10.1073/pnas.0705483104.
31. Plamondon JA, Harris MJ, Mager DL, Gagnier L, Juriloff DM. The *clf2* gene has an epigenetic role in the multifactorial etiology of cleft lip and palate in the A/WySn mouse strain. Birth Defects Res A Clin Mol Teratol. 2011;91:716–27. https://doi.org/10.1002/bdra.20788.
32. Swanzey E, McNamara TF, Apostolou E, Tahiliani M, Stadtfeld M. A Susceptibility Locus on Chromosome 13 Profoundly Impacts the Stability of Genomic Imprinting in Mouse Pluripotent Stem Cells. Cell Rep. 2020;30:3597-3604.e3. https://doi.org/10.1016/j.celrep.2020.02.073. Elsevier.
33. Treger RS, Pope SD, Kong Y, Tokuyama M, Taura M, Iwasaki A. The lupus susceptibility locus *Sgp3* encodes the suppressor of endogenous retrovirus expression SNERV. Immunity. 2019;50:334–47. https://doi.org/10.1016/j.immuni.2018.12.022.
34. Skelly DA, Czechanski A, Byers C, Aydin S, Spruce C, Olivier C, et al. Mapping the Effects of Genetic Variation on Chromatin State and Gene Expression Reveals Loci That Control Ground State Pluripotency. Cell Stem Cell. 2020;27:459-469.e8. https://doi.org/10.1016/j.stem.2020.07.005. Elsevier.
35. Cheung VG, Spielman RS. Genetics of human gene expression: mapping DNA variants that influence gene expression. Nat Rev Genet. 2009;10:595–604. https://doi.org/10.1038/nrg2630.
36. Mattioli K, Oliveros W, Gerhardinger C, Andergassen D, Maass PG, Rinn JL, et al. Cis and trans effects differentially contribute to the evolution of promoters and enhancers. Genome Biol. 2020;21:210. https://doi.org/10.1186/s13059-020-02110-3.
37. Fullwood MJ, Wei C-L, Liu ET, Ruan Y. Next-generation DNA sequencing of paired-end tags (PET) for transcriptome and genome analyses. Genome Res. 2009;19:521–32. https://doi.org/10.1101/gr.074906.107. Cold Spring Harbor Lab.
38. Mifsud B, Tavares-Cadete F, Young AN, Sugar R, Schoenfelder S, Ferreira L, et al. Mapping long-range promoter contacts in human cells with high-resolution capture Hi-C. Nat Genet Nature Publishing Group. 2015;47:598–606. https://doi.org/10.1038/ng.3286.
39. Mumbach MR, Rubin AJ, Flynn RA, Dai C, Khavari PA, Greenleaf WJ, et al. HiChIP: efficient and sensitive analysis of protein-directed genome architecture. Nat Methods Nature Publishing Group. 2016;13:919–22. https://doi.org/10.1038/nmeth.3999.
40. Fang R, Yu M, Li G, Chee S, Liu T, Schmitt AD, et al. Mapping of long-range chromatin interactions by proximity ligation-assisted ChIP-seq. Cell Res. 2016;26:1345–8. https://doi.org/10.1038/cr.2016.137. Nature Publishing Group.
41. Krijger PHL, Geeven G, Bianchi V, Hilvering CRE, de Laat W. 4C-seq from beginning to end: A detailed protocol for sample preparation and data analysis. Methods. 2020;170:17–32. https://doi.org/10.1016/j.ymeth.2019.07.014.
42. van Berkum NL, Lieberman-Aiden E, Williams L, Imakaev M, Gnirke A, Mirny LA, et al. Hi-C: A Method to Study the Three-dimensional Architecture of Genomes. J Vis Exp. 2010;1869. https://doi.org/10.3791/1869

43. Beagrie RA, Scialdone A, Schueler M, Kraemer DCA, Chotalia M, Xie SQ, et al. Complex multi-enhancer contacts captured by genome architecture mapping. Nature. 2017;543:519–24. https://doi.org/10.1038/nature21411. Nature Publishing Group.
44. Dekker J, Mirny L. The 3D Genome as Moderator of Chromosomal Communication. Cell. 2016;164:1110–21. https://doi.org/10.1016/j.cell.2016.02.007.
45. Bortle KV, Corces VG. Nuclear Organization and Genome Function. Annu Rev Cell Dev Biol. 2012;28:163–87. https://doi.org/10.1146/annurev-cellbio-101011-155824.
46. Bonev B, Cavalli G. Organization and function of the 3D genome. Nat Rev Genet. 2016;17:661–78. https://doi.org/10.1038/nrg.2016.112.
47. Gorkin DU, Leung D, Ren B. The 3D Genome in Transcriptional Regulation and Pluripotency. Cell Stem Cell. 2014;14:762–75. https://doi.org/10.1016/j.stem.2014.05.017.
48. Hug CB, Vaquerizas JM. The Birth of the 3D Genome during Early Embryonic Development. Trends Genet. 2018;34:903–14. https://doi.org/10.1016/j.tig.2018.09.002. Elsevier.
49. Carter D, Chakalova L, Osborne CS, Dai Y-F, Fraser P. Long-range chromatin regulatory interactions in vivo. Nat Genet. 2002;32:623–6. https://doi.org/10.1038/ng1051.
50. Li G, Ruan X, Auerbach RK, Sandhu KS, Zheng M, Wang P, et al. Extensive Promoter-Centered Chromatin Interactions Provide a Topological Basis for Transcription Regulation. Cell. 2012;148:84–98. https://doi.org/10.1016/j.cell.2011.12.014.
51. Sanyal A, Lajoie BR, Jain G, Dekker J. The long-range interaction landscape of gene promoters. Nature. 2012;489:109–13. https://doi.org/10.1038/nature11279. Nature Publishing Group.
52. Tolhuis B, Palstra R-J, Splinter E, Grosveld F, de Laat W. Looping and Interaction between Hypersensitive Sites in the Active β-globin Locus. Mol Cell. 2002;10:1453–65. https://doi.org/10.1016/S1097-2765(02)00781-5.
53. Dixon JR, Selvaraj S, Yue F, Kim A, Li Y, Shen Y, et al. Topological domains in mammalian genomes identified by analysis of chromatin interactions. Nature. 2012;485:376–80. https://doi.org/10.1038/nature11082. Nature Publishing Group.
54. Nora EP, Lajoie BR, Schulz EG, Giorgetti L, Okamoto I, Servant N, et al. Spatial partitioning of the regulatory landscape of the X-inactivation centre. Nature. 2012;485:381–5. https://doi.org/10.1038/nature11049. Nature Publishing Group.
55. Smith EM, Lajoie BR, Jain G, Dekker J. Invariant TAD boundaries constrain cell-type-specific looping interactions between promoters and distal elements around the *CFTR* locus. Am J Hum Genet. 2016;98:185–201. https://doi.org/10.1016/j.ajhg.2015.12.002.
56 Martin P, McGovern A, Orozco G, Duffus K, Yarwood A, Schoenfelder S, et al. Capture Hi-C reveals novel candidate genes and complex long-range interactions with related autoimmune risk loci. Nat Commun. 2015;6:10069. https://doi.org/10.1038/ncomms10069. Nature Publishing Group.
57. Franke M, Ibrahim DM, Andrey G, Schwarzer W, Heinrich V, Schöpflin R, et al. Formation of new chromatin domains determines pathogenicity of genomic duplications. Nature. 2016;538:265–9. https://doi.org/10.1038/nature19800. Nature Publishing Group.
58. Lupiáñez DG, Kraft K, Heinrich V, Krawitz P, Brancati F, Klopocki E, et al. Disruptions of topological chromatin domains cause pathogenic rewiring of gene-enhancer interactions. Cell. 2015;161:1012–25. https://doi.org/10.1016/j.cell.2015.04.004.
59. Cova G, Glaser J, Schöpflin R, Prada-Medina CA, Ali S, Franke M, et al. Combinatorial effects on gene expression at the Lbx1/Fgf8 locus resolve split-hand/foot malformation type 3. Nat Commun. 2023;14:1475. https://doi.org/10.1038/s41467-023-37057-z. Nature Publishing Group.
60. Gorkin DU, Qiu Y, Hu M, Fletez-Brant K, Liu T, Schmitt AD, et al. Common DNA sequence variation influences 3-dimensional conformation of the human genome. Genome Biol. 2019;20:255. https://doi.org/10.1186/s13059-019-1855-4.
61. Peng Y, Xiong D, Zhao L, Ouyang W, Wang S, Sun J, et al. Chromatin interaction maps reveal genetic regulation for quantitative traits in maize. Nat Commun. 2019;10:2632. https://doi.org/10.1038/s41467-019-10602-5.
62. Zhao L, Wang S, Cao Z, Ouyang W, Zhang Q, Xie L, et al. Chromatin loops associated with active genes and heterochromatin shape rice genome architecture for transcriptional regulation. Nat Commun. 2019;10:3640. https://doi.org/10.1038/s41467-019-11535-9.
63. Schoenfelder S, Javierre B-M, Furlan-Magaril M, Wingett SW, Fraser P. Promoter Capture Hi-C: High-resolution, Genome-wide Profiling of Promoter Interactions. JoVE (J Visual Exp). 2018;e57320. https://doi.org/10.3791/57320
64. Hagège H, Klous P, Braem C, Splinter E, Dekker J, Cathala G, et al. Quantitative analysis of chromosome conformation capture assays (3C-qPCR). Nat Protoc. 2007;2:1722–33. https://doi.org/10.1038/nprot.2007.243.
65. Friedman JR, Fredericks WJ, Jensen DE, Speicher DW, Huang XP, Neilson EG, et al. KAP-1, a novel corepressor for the highly conserved KRAB repression domain. Genes Dev. 1996;10:2067–78. https://doi.org/10.1101/gad.10.16.2067. Cold Spring Harbor Lab.
66. Moosmann P, Georgiev O, Thiesen H-J, Hagmann M, Schaffner W. Silencing of RNA Polymerases II and III-Dependent Transcription by the KRAB Protein Domain of KOX1, a Krüppel-Type Zinc Finger Factor. Biol Chem De Gruyter. 1997;378:669–78. https://doi.org/10.1515/bchm.1997.378.7.669.
67. Guo Y, Xue Z, Yuan R, Li JJ, Pastor WA, Liu W. RAD: a web application to identify region associated differentially expressed genes. Bioinformatics. 2021;37:2741–3. https://doi.org/10.1093/bioinformatics/btab075.
68. Tian J, Keller MP, Broman AT, Kendziorski C, Yandell BS, Attie AD, et al. The Dissection of Expression Quantitative Trait Locus Hotspots. Genetics. 2016;202:1563–74. https://doi.org/10.1534/genetics.115.183624.
69. Di Giammartino DC, Kloetgen A, Polyzos A, Liu Y, Kim D, Murphy D, et al. KLF4 is involved in the organization and regulation of pluripotency-associated three-dimensional enhancer networks. Nat Cell Biol. 2019;21:1179–90. https://doi.org/10.1038/s41556-019-0390-6.
70. Greenwald WW, Li H, Benaglio P, Jakubosky D, Matsui H, Schmitt A, et al. Subtle changes in chromatin loop contact propensity are associated with differential gene regulation and expression. Nat Commun. 2019;10:1054, 1054. https://doi.org/10.1038/s41467-019-08940-5.

71. Bond ML, Davis ES, Quiroga IY, Dey A, Kiran M, Love MI, et al. Chromatin loop dynamics during cellular differentiation are associated with changes to both anchor and internal regulatory features. Genome Res. 2023;33:1258–68. https://doi.org/10.1101/gr.277397.122.
72. Ray-Jones H, Sung CK, Chan LT, Haglund A, Artemov P, Della Rosa M, et al. Genetic coupling of enhancer activity and connectivity in gene expression control. Nat Commun. 2025;16:970. https://doi.org/10.1038/s41467-025-55900-3. Nature Publishing Group.
73. Shi C, Zhao D, Butler J, Frantzeskos A, Rossi S, Ding J, et al. Multi-omics analysis in primary T cells elucidates mechanisms behind disease-associated genetic loci. Genome Biol. 2025;26:26, 26. https://doi.org/10.1186/s13059-025-03492-y.
74. Thiesen HJ. Multiple genes encoding zinc finger domains are expressed in human T cells. New Biol. 1990;2:363–74.
75 Bellefroid EJ, Poncelet DA, Lecocq PJ, Revelant O, Martial JA. The evolutionarily conserved Krüppel-associated box domain defines a subfamily of eukaryotic multifingered proteins. Proc Natl Acad Sci U S A. 1991;88:3608–12. https://doi.org/10.1073/pnas.88.9.3608.
76. Schultz DC, Ayyanathan K, Negorev D, Maul GG, Rauscher FJ. SETDB1: a novel KAP-1-associated histone H3, lysine 9-specific methyltransferase that contributes to HP1-mediated silencing of euchromatic genes by KRAB zinc-finger proteins. Genes Dev. 2002;16:919–32. https://doi.org/10.1101/gad.973302.
77. Lupo A, Cesaro E, Montano G, Zurlo D, Izzo P, Costanzo P. KRAB-Zinc Finger Proteins: A Repressor Family Displaying Multiple Biological Functions. Curr Genomics. 2013;14:268–78. https://doi.org/10.2174/13892029113149990002.
78. Sripathy SP, Stevens J, Schultz DC. The KAP1 Corepressor Functions To Coordinate the Assembly of De Novo HP1-Demarcated Microenvironments of Heterochromatin Required for KRAB Zinc Finger Protein-Mediated Transcriptional Repression. Mol Cell Biol. 2006;26:8623–38. https://doi.org/10.1128/MCB.00487-06.
79. Francis BA, Gozashti L, Costello K, Kasahara T, Harringmeyer OS, Lilue J, et al. Complete genome assemblies of two mouse subspecies reveal structural diversity of telomeres and centromeres. Nat Genet. 2025;57:2852–62. https://doi.org/10.1038/s41588-025-02367-z. Nature Publishing Group.
80. Bruno M, Farhana SM, Mitra A, Costello K, Watkins-Chow DE, Logsdon GA, et al. Young KRAB-zinc finger gene clusters are highly dynamic incubators of ERV-driven genetic heterogeneity in mice. Nat Commun. 2025;16:9608. https://doi.org/10.1038/s41467-025-64609-2. Nature Publishing Group.
81. Groner AC, Meylan S, Ciuffi A, Zangger N, Ambrosini G, Dénervaud N, et al. KRAB–Zinc Finger Proteins and KAP1 Can Mediate Long-Range Transcriptional Repression through Heterochromatin Spreading. PLOS Genetics. 2010;6:e1000869. https://doi.org/10.1371/journal.pgen.1000869. Public Library of Science.
82. Larson MH, Gilbert LA, Wang X, Lim WA, Weissman JS, Qi LS. CRISPR interference (CRISPRi) for sequence-specific control of gene expression. Nat Protoc. 2013;8:2180–96. https://doi.org/10.1038/nprot.2013.132.
83. Imbeault M, Helleboid P-Y, Trono D. KRAB zinc-finger proteins contribute to the evolution of gene regulatory networks. Nature Nature Publishing Group. 2017;543:550–4. https://doi.org/10.1038/nature21683.
84. Hansen TJ, Fong SL, Day JK, Capra JA, Hodges E. Human gene regulatory evolution is driven by the divergence of regulatory element function in both cis and trans. Cell Genomics. Elsevier; 2024;4. https://doi.org/10.1016/j.xgen.2024.100536. Cited 2025 Sept 25.
85. Becker JS, Nicetto D, Zaret KS. H3K9me3-Dependent Heterochromatin: Barrier to Cell Fate Changes. Trends Genet. 2016;32:29–41. https://doi.org/10.1016/j.tig.2015.11.001.
86. Soufi A, Donahue G, Zaret KS. Facilitators and Impediments of the Pluripotency Reprogramming Factors' Initial Engagement with the Genome. Cell. 2012;151:994–1004. https://doi.org/10.1016/j.cell.2012.09.045.
87. Kaemena DF, Yoshihara M, Beniazza M, Ashmore J, Zhao S, Bertenstam M, et al. B1 SINE-binding ZFP266 impedes mouse iPSC generation through suppression of chromatin opening mediated by reprogramming factors. Nat Commun. 2023;14:488. https://doi.org/10.1038/s41467-023-36097-9. Nature Publishing Group.
88. Kim S-K, Seo S, Stein-O'Brien G, Jaishankar A, Ogawa K, Micali N, et al. Individual variation in the emergence of anterior-to-posterior neural fates from human pluripotent stem cells. Stem Cell Rep. 2024;19:1336–50. https://doi.org/10.1016/j.stemcr.2024.07.004.
89. Perdomo-Sabogal Á, Nowick K. Genetic Variation in Human Gene Regulatory Factors Uncovers Regulatory Roles in Local Adaptation and Disease. Genome Biol Evol. 2019;11:2178–93. https://doi.org/10.1093/gbe/evz131.
90. Sigmon JS, Blanchard MW, Baric RS, Bell TA, Brennan J, Brockmann GA, et al. Content and Performance of the MiniMUGA Genotyping Array: A New Tool To Improve Rigor and Reproducibility in Mouse Research. Genetics. 2020;216:905–30. https://doi.org/10.1534/genetics.120.303596.
91. Czechanski A, Byers C, Greenstein I, Schrode N, Donahue LR, Hadjantonakis A-K, et al. Derivation and characterization of mouse embryonic stem cells (mESCs) from permissive and non-permissive strains. Nat Protoc. 2014;9:559–74. https://doi.org/10.1038/nprot.2014.030.
92. Corces MR, Buenrostro JD, Wu B, Greenside PG, Chan SM, Koenig JL, et al. Lineage-specific and single-cell chromatin accessibility charts human hematopoiesis and leukemia evolution. Nat Genet. 2016;48:1193–203. https://doi.org/10.1038/ng.3646. Nature Publishing Group.
93. Billings T, Parvanov ED, Baker CL, Walker M, Paigen K, Petkov PM. DNA binding specificities of the long zinc-finger recombination protein PRDM9. Genome Biol. 2013;14:R35. https://doi.org/10.1186/gb-2013-14-4-r35.
94 Belaghzal H, Dekker J, Gibcus JH. Hi-C 2.0: An optimized Hi-C procedure for high-resolution genome-wide mapping of chromosome conformation. Methods. 2017;123:56–65. https://doi.org/10.1016/j.ymeth.2017.04.004.
95. Dovetail-HiChip-MNase-Kit-Version-2.0.pdf. https://cantatabio.com/wp-content/uploads/2023/12/Dovetail-HiChip-MNase-Kit-Version-2.0.pdf. Accessed 7 July 2025. Cited 2025 July 7.
96. Bolger AM, Lohse M, Usadel B. Trimmomatic: a flexible trimmer for Illumina sequence data. Bioinformatics. 2014;30:2114–20. https://doi.org/10.1093/bioinformatics/btu170.
97. Yalcin B, Wong K, Agam A, Goodson M, Keane TM, Gan X, et al. Sequence based characterization of structural variation in the mouse genome. Nature. 2011;477:326–9. https://doi.org/10.1038/nature10432.
98. Pertea M, Kim D, Pertea G, Leek JT, Salzberg SL. Transcript-level expression analysis of RNA-seq experiments with HISAT, StringTie, and Ballgown. Nat Protoc. 2016;11:1650–67. https://doi.org/10.1038/nprot.2016.095.
99. Picard Tools - By Broad Institute. https://broadinstitute.github.io/picard/. Accessed 9 July 2025. Cited 2025 July 9.

100. Zhang Y, Liu T, Meyer CA, Eeckhoute J, Johnson DS, Bernstein BE, et al. Model-based Analysis of ChIP-Seq (MACS). Genome Biol. 2008;9:R137. https://doi.org/10.1186/gb-2008-9-9-r137.
101. Quinlan AR, Hall IM. BEDTools: a flexible suite of utilities for comparing genomic features. Bioinformatics. 2010;26:841–2. https://doi.org/10.1093/bioinformatics/btq033.
102. Robinson MD, McCarthy DJ, Smyth GK. edgeR: a Bioconductor package for differential expression analysis of digital gene expression data. Bioinformatics. 2010;26:139–40. https://doi.org/10.1093/bioinformatics/btp616.
103. Gel B, Serra E. karyoploteR: an R/Bioconductor package to plot customizable genomes displaying arbitrary data. Bioinformatics. 2017;33:3088–90. https://doi.org/10.1093/bioinformatics/btx346.
104. Li H, Durbin R. Fast and accurate short read alignment with Burrows-Wheeler transform. Bioinformatics. 2009;25:1754–60. https://doi.org/10.1093/bioinformatics/btp324.
105. Raghupathy N, Choi K, Vincent MJ, Beane GL, Sheppard KS, Munger SC, et al. Hierarchical analysis of RNA-seq reads improves the accuracy of allele-specific expression. Bioinformatics. 2018;34:2177–84. https://doi.org/10.1093/bioinformatics/bty078.
106. Langmead B, Trapnell C, Pop M, Salzberg SL. Ultrafast and memory-efficient alignment of short DNA sequences to the human genome. Genome Biol [Internet]. Springer Science and Business Media LLC; 2009;10. https://doi.org/10.1186/gb-2009-10-3-r25. Cited 2025 July 7.
107. Servant N, Varoquaux N, Lajoie BR, Viara E, Chen C-J, Vert J-P, et al. HiC-Pro: an optimized and flexible pipeline for Hi-C data processing. Genome Biol. 2015;16:259. https://doi.org/10.1186/s13059-015-0831-x.
108. Lareau CA, Aryee MJ. hichipper: a preprocessing pipeline for calling DNA loops from HiChIP data. Nat Methods. 2018;15:155–6. https://doi.org/10.1038/nmeth.4583. Nature Publishing Group.
109. Lareau CA, Aryee MJ. diffloop: a computational framework for identifying and analyzing differential DNA loops from sequencing data. Bioinformatics. 2018;34:672–4. https://doi.org/10.1093/bioinformatics/btx623.
110. Love MI, Huber W, Anders S. Moderated estimation of fold change and dispersion for RNA-seq data with DESeq2. Genome Biol [Internet]. Springer Science and Business Media LLC; 2014;15. https://doi.org/10.1186/s13059-014-0550-8. Cited 2025 July 7.
111. HiChIP 0.1 documentation. https://hichip.readthedocs.io/en/latest/before_you_begin.html. Accessed 7 July 2025. Cited 2025 July 7.
112. Open2C, Abdennur N, Fudenberg G, Flyamer IM, Galitsyna AA, Goloborodko A, et al. Pairtools: From sequencing data to chromosome contacts. Ay F, editor. PLoS Comput Biol. 2024;20:e1012164. https://doi.org/10.1371/journal.pcbi.1012164. Public Library of Science (PLoS).
113. Li H, Handsaker B, Wysoker A, Fennell T, Ruan J, Homer N, et al. The Sequence Alignment/Map format and SAMtools. Bioinformatics. 2009;25:2078–9. https://doi.org/10.1093/bioinformatics/btp352.
114 Bhattacharyya S, Chandra V, Vijayanand P, Ay F. Identification of significant chromatin contacts from HiChIP data by FitHiChIP. Nat Commun. 2019;10:4221. https://doi.org/10.1038/s41467-019-11950-y. Nature Publishing Group.
115. Gel B, Díez-Villanueva A, Serra E, Buschbeck M, Peinado MA, Malinverni R. regioneR: an R/Bioconductor package for the association analysis of genomic regions based on permutation tests. Bioinformatics. 2016;32:289–91. https://doi.org/10.1093/bioinformatics/btv562.
116. Fortin HJ, Struba AZ, Bustan A, Baker CL. Trans-regulation of heterochromatin underlies genetic variation in 3D genome contacts. ATAC-seq, H3K27ac ChIP-seq, H3K9me3 ChIP-seq, RNA-seq, and HiChIP datasets. Gene Expression Omnibus. 2026. https://www.ncbi.nlm.nih.gov/geo/query/acc.cgi?acc=GSE312918.
117. Baker C. Genome-wide maps of H3K4me3 in C57BL6/J, DBA/2J, and BXD lines for male germ cells, hepatocytes, cardiomyocytes, and mouse ESCs. H3K4me3 ChIP-seq dataset. Gene Expression Omnibus. 2019. https://www.ncbi.nlm.nih.gov/geo/query/acc.cgi?acc=GSE113192.
118. Baker C, Byers C. Genetic control of pluripotency epigenome informs differentiation bias in mouse embryonic stem cells. ATAC-seq and RNA-seq datasets. Gene Expression Omnibus. 2021. https://www.ncbi.nlm.nih.gov/geo/query/acc.cgi?acc=GSE164935.

Publisher's Note